

A Soft Motion Compensation System for Cranial Cancer Radiation Therapy.

By: Olalekan Ogunmolu
3620 Hamilton Walk, #183
Department of Radiation Oncology
Perelman School of Medicine
The University of Pennsylvania
Phone: +215-898-5088
Email: olalekan.ogunmolu@pennmedicine.upenn.edu

Faculty Mentor: Rodney D. Wiersma, PhD, DABR
3620 Hamilton Walk, #183
Department of Radiation Oncology
Perelman School of Medicine
The University of Pennsylvania
Email: rodney.wiersma@pennmedicine.upenn.edu

January 20, 2020

Background

Introduction: Cancer is an existential burden on rich and poor nations alike. At a cost of \$147.3 billion, it consumes about 4.2% of overall health care spending in the United States alone [2]. Radiation Therapy (RT), in conjunction with surgery and chemotherapy, can be an invaluable single cancer treatment modality: it is cost-effective (accounting for only 5% of the total cost of cancer care [25]), and given its advanced mode of radiation production and delivery, RT accounts for half of all cancer treatments [3].

An open problem in radiation therapy (RT) is keeping the patient immobile during treatment: $< 2\text{mm}$ from those in the pre-calculated *treatment planning parameters* [28]. The state-of-the-art in clinics utilizes a rigid frame or mask (Fig. 1) to achieve this. In frame-based systems (Fig. 1, left inset), a metallic frame is screwed onto the patient's skull and then bolted to a treatment table. Owing to its invasiveness, the associated discomfort to the patient has been linked to poor patient compliance and subpar clinical efficacy. Even so, frames are not useful in multiple RT deliveries owing to the requirement for daily attachment and removal of the frame. With thermoplastics (Fig. 1, right inset),

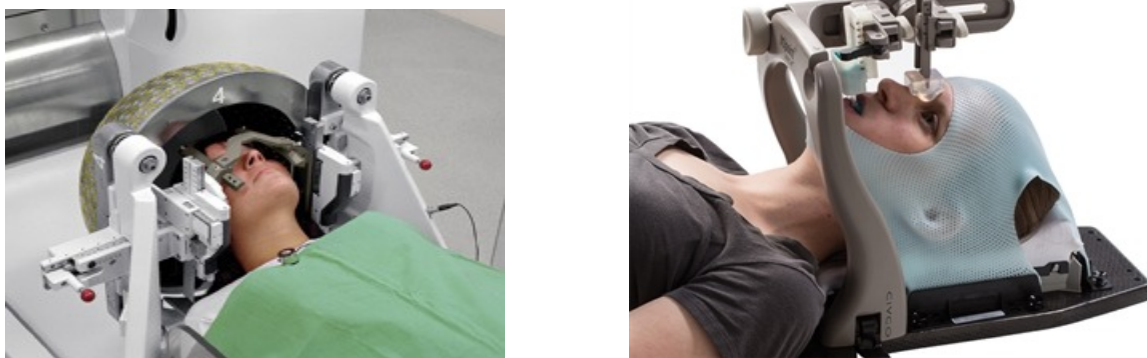


Figure 1: (Left) Frame and mask immobilization in RT (Right).

there is often decreased positioning accuracy owing to the plastic properties of the mask. For tumors near critical structures such as the brain stem or for newer treatment modalities such as single isocenter multiple-target stereotactic radiosurgery (SRS), which are highly sensitive to rotational head motion errors, this is not a feasible positioning method.

Frameless Positioning Systems and Limitations: Because of the downsides of frame/mask-based systems, frameless and maskless immobilization systems are an active area of research. The CyberKnife system [1], while having an advanced mode of beam repositioning and radiation delivery, still requires a frame or mask – being incapable of real-time closed-loop feedback head motion correction when the treatment beam is on. The CyberKnife Synchrony, while capable of precise, non-surgical tumor and lesions treatment in SRS and stereotactic body radiotherapy, only executes *a-priori* trajectories and is only FDA-approved for lung tumors' treatment. Correction requirements in these systems require far less accuracy, typically $< 5\text{mm}$ [9] than brain targets. Moreover, real-time closed-loop head motion compensation for the CyberKnife system is inhibited by its high load-to-weight ratio which indirectly affects its repeatability: its links inherently magnify errors from shoulder out to the end-effector, thereby hampering its use for sophisticated control strategies that may minimize or eliminate load-dependent errors.

Even so, the significant efforts that have been put in research labs on using rigid Stewart-Gough platforms for patient immobilization (such as the works of [4, 8, 12]) have drawbacks: (i) given their constant-curvature end-effectors/platforms, they are incapable of providing sophisticated manipulation e.g. for the respiratory motions that often induce deviation from a target; (ii) and being made out of rigid bodies, the attenuation of ionizing radiation dose has to be factored into treatment plans when these systems become commissioned.

Approach

Aims: Given the accurate dose targeting requirement for SRS, it is important to (i) be able to correct patient motion-deviation in real-time during treatment; (ii) achieve aim (i) with components that do not attenuate the radiation beam (unlike rigid mechanisms that have been proposed by [4, 8] and [12]); and (iii) provide comfort to the patient while achieving these aims.

To our knowledge, there is no available technology for realizing these objectives in clinics today. Soft matter [5], is an attractive actuation mechanism for solving major automation problems given its compliance. Their many degrees-of-freedom (DOFs) however inhibit their controllability [26]. My preliminary work on the design and vision-based control of soft manipulators has demonstrated the feasibility of soft robot mechanisms for real-time cranial control in simulated and test scenarios [17, 18, 21, 22]. Here, we propose a soft continuum, compliant and configurable (*C3*) complete immobilization system for 6-DOF real-time cranial motion correction [19, 20] illustrated in Fig. 2 and 3: if a patient (in)voluntarily deviates from a treatment plan during treatment, we propose suitable real-time adaptive controllers that will actuate these *C3* soft robots for head motion correction while minimizing hard shocks to the patient and assuring patient comfort. In addition, their compliance the actuators would allow for MRI-based RT where dose sensitivity, patient comfort, and treatment efficacy are paramount. Our soft actuation system is bio-inspired from Cephalopods' behavior and we highlight the proposed hardware and control design to bring to fruition this technology. *To our knowledge, there is no available technology today with the capability of MRI and *C3*-based real-time head position stabilization compared to our proposed system.*

Hardware Design: Inspired by the behavior of the papillae of certain cephalopods (octopus, cuttlefish and mollusks) which can transform their physical texture from 2D to 3D in less than 2 seconds [6, 7], we propose the experiments to reproduce this behavior in soft actuators (Fig. 2) similar to the Gaussian deformations reproduced in [24]. These soft

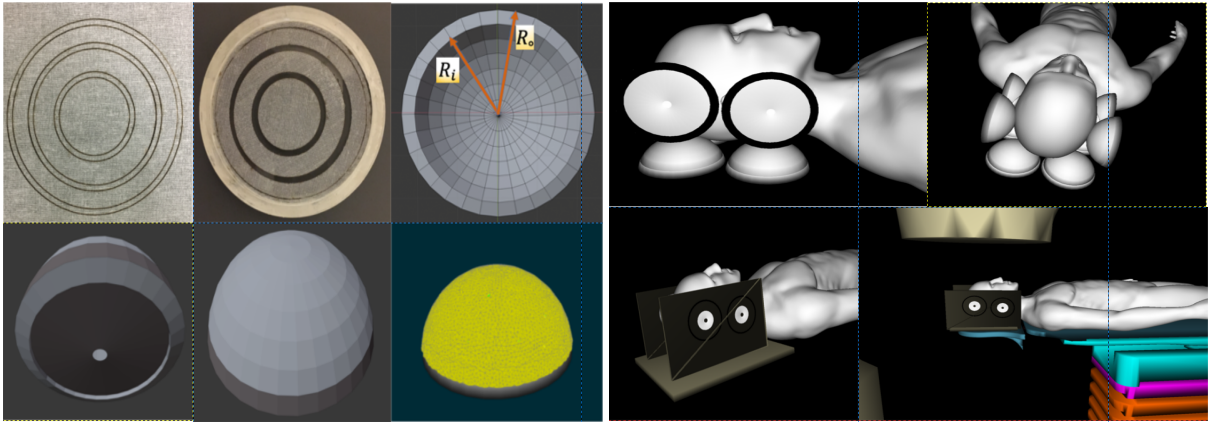


Figure 2: Soft Robot Fabrication and Modeling Description.

actuators are kinematically arranged to reproduce desired real-time 6-DOF motion compensation in RT as illustrated in Fig. 3.

We now describe the preliminary experiments laid out in the left collage of Fig. 2. A non-woven fabric, laser cut into circular patterns (top-left), is laid onto uncured silicone in a mold (top-middle). Upon application of air pressure, the silicone layer deforms based on the circumferentially-constrained and radially symmetric pattern (CCOARSE) [23] just as a balloon would elongate along its axial direction if a rope is tied around its circumferential axis. The behavior of the soft robot after cure under the application of pneumatic pressure (top-right). The soft robot is thereafter laid onto a carbon fiber fitting which is stuffed with styrofoam to prevent dose attenuation (bottom-left and middle); this is similar to the support systems used in clinics from CDR Systems Canada®. The hole in the middle allows for hose insertion for air pressurization. Finite element model of the soft robot for simulation purposes (bottom right).

In the right inset of the figure, the soft domes are positioned around a patient's cranial region (top) who lies supinely on the treatment couch (bottom-right) while the radiation beam is being delivered on to their cranial cancer regions (bottom). The soft robots are again enclosed in adjustable carbon fiber rectangular cuttings that are stuffed with styrofoam to prevent dose attenuation and free-fall of the soft robots when at rest.

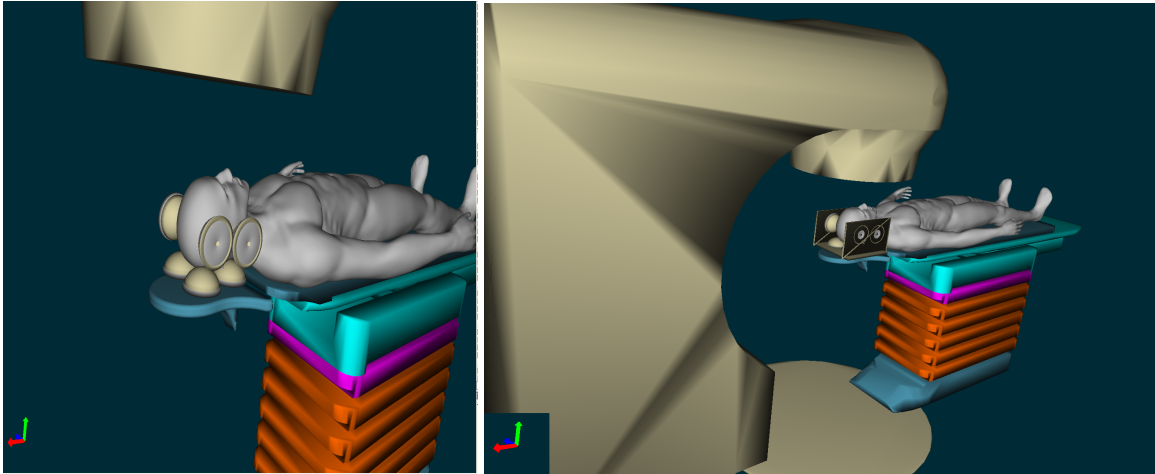


Figure 3: *Left:* Close-up view of proposed setup without enclosing casing. *Right:* Overall setup.

Mathematical Model: The effect of deformation of the soft robots on head motion will be controlled using a vision-based feedback control mechanism that adjusts the amount of air pressurization in the soft domes based on patient deviation from parameters in the treatment plan. Using differential kinematics and finite elastic deformation as delineated in [16], we relate the contact forces on the head with the soft robot's deformation and through inverse dynamics, we derive the motions that govern the cranial region of the head.

Control Proposal: The control algorithm will rely on prehensile multi-body systems [14, 15] and nonlinear feedback control [10] so as to optimize an appropriate trajectory [11, 27] for the head motion during treatment regimes. We will leverage our proposed trajectory optimization for SRS motion correction systems [13] to control the head in real-time.

Significance

Soft robots are promising actuation systems but have found few practical application to date owing to their modeling and control difficulty [5]. Given our outlined fabrication procedure and elaborate mathematical model [16, 19] and trajectory optimization algorithm [13], we propose to edge open the soft actuators application door further and pave the way for other researchers to exploit the use of soft actuators in other biomedical research. Owing to the novel fabrication and design of the mechanism, it avoids the radiation attenuation issues associated with rigid Stewart-Gough platforms being explored in research labs today [4, 8]. This research will show that rigid multi-body systems can be replaced with cheap soft components to realize precise control based on the method which we have devised for their model, fabrication and control. To our knowledge, ours is the first to exploit parallel kinematic arrangements of novel bio-inspired soft actuators for motion compensation in radiation oncology. The modeling, design and hardware verification gained from this research will be disseminated in top journals to improve biomedical radiation treatment planning research ecosystem.

Bibliography

- [1] Adler, J.R., Cox, R.S.: Preliminary clinical experience with the cyberknife: Image-guided stereotactic radiosurgery. In: *Radiosurgery 1995*, vol. 1, pp. 316–326. Karger Publishers (1996)
- [2] American Cancer Society: Cancer facts and figures (2019). URL <https://www.cancer.org/research/cancer-facts-statistics/all-cancer-facts-figures/cancer-facts-figures-2019.html>. Accessed October 23, 2019
- [3] Baskar, R., Lee, K.A., Yeo, R., Yeoh, K.W.: Cancer and radiation therapy: current advances and future directions. *International journal of medical sciences* **9**(3), 193 (2012)
- [4] Belcher, A.: Patient Motion Management with 6-DOF Robotics for Frameless and Maskless Stereotactic Radio-surgery. Ph.D. thesis, The University of Chicago (2017)
- [5] George Thuruthel, T., Ansari, Y., Falotico, E., Laschi, C.: Control Strategies for Soft Robotic Manipulators: A Survey. *Soft Robotics* **5**(2), 149–163 (2018). DOI 10.1089/soro.2017.0007
- [6] Hanlon, R.T., Messenger, J.B.: Adaptive coloration in young cuttlefish (*sepia officinalis* l.): the morphology and development of body patterns and their relation to behaviour. *Philosophical Transactions of the Royal Society of London. B, Biological Sciences* **320**(1200), 437–487 (1988)
- [7] Hanlon, R.T., Messenger, J.B.: *Cephalopod behaviour*. Cambridge University Press (2018)
- [8] Herrmann, C., Ma, L., Schilling, K.: Model Predictive Control For Tumor Motion Compensation In Robot Assisted Radiotherapy. *IFAC Proceedings Volumes* **44**(1), 5968–5973 (2011)
- [9] Keall, P.J., Mageras, G.S., Balter, J.M., Emery, R.S., Forster, K.M., Jiang, S.B., Kapatoes, J.M., Low, D.A., Murphy, M.J., Murray, B.R., et al.: The Management of Respiratory Motion in Radiation Oncology Report of AAPM Task Group 76 A. *Medical physics* **33**(10), 3874–3900 (2006)
- [10] Khalil, H.K.: *Nonlinear systems*. Upper Saddle River (2002)
- [11] Levine, S., Koltun, V.: Learning complex neural network policies with trajectory optimization. In: *International Conference on Machine Learning*, pp. 829–837 (2014)
- [12] Liu, X., Belcher, A.H., Grelewicz, Z., Wiersma, R.D.: Robotic stage for head motion correction in stereotactic radiosurgery. In: *2015 American Control Conference (ACC)*, pp. 5776–5781. IEEE (2015)
- [13] Liu, X., Wiersma, R.D.: Optimization based trajectory planning for real-time 6DoF robotic patient motion compensation systems. *PloS one* **14**(1), e0210,385 (2019)
- [14] Murray, R.M., Sastry, S.: Grasping and Manipulation using Multifingered Robot Hands. In: *Proceedings of Symposia in Applied Mathematics*, vol. 41, pp. 329–335 (1990)
- [15] Nguyen, V.D.: Constructing force-closure grasps. *The International Journal of Robotics Research* **7**(3), 3–16 (1988)
- [16] Ogunmolu, O.: A Generalized Neural Constitutive Framework for the Kinematics and Kinetics of In-Parallel-Actuated Soft Robot Manipulators (2020). URL <https://scriptedonachip.com/downloads/Papers/kinecontrol.pdf>
- [17] Ogunmolu, O., Gans, N., Jiang, S., Gu, X.: An Image Guided Soft Robotic Patient Positioning System for Maskless Head And Neck Cancer Radiotherapy: A Proof of Concept Study. *Medical Physics: The International Journal of Medical Physics Research and Practice* **42**, 3266–3266 (2015)
- [18] Ogunmolu, O., Kulkarni, A., Tadesse, Y., Gu, X., Jiang, S., Gans, N.: Soft-neuroadapt: A 3-dof neuro-adaptive patient pose correction system for frameless and maskless cancer radiotherapy. In: *IEEE/RSJ International Conference on Intelligent Robots and Systems (IROS)*, Vancouver, BC, CA, pp. 3661–3668. IEEE (2017)
- [19] Ogunmolu, O., Liu, X., Wiersma, R.: Mechanism and Constitutive Model of a Continuum Robot for Head and Neck Cancer Radiotherapy (2019)
- [20] Ogunmolu, O.P.: A Multi-DOF Soft Robot Mechanism for Patient Motion Correction and Beam Orientation Selection in Cancer Radiation Therapy. Ph.D. thesis, The University of Texas at Dallas; UT Southwestern Medical Center (2019)
- [21] Ogunmolu, O.P., Gu, X., Jiang, S., Gans, N.R.: A real-time, soft robotic patient positioning system for maskless head-and-neck cancer radiotherapy: An initial investigation. In: *Automation Science and Engineering (CASE), 2015 IEEE International Conference on*, Gothenburg, Sweden, pp. 1539–1545. IEEE (2015)

- [22] Ogunmolu, O.P., Gu, X., Jiang, S., Gans, N.R.: Vision-based control of a soft robot for maskless head and neck cancer radiotherapy. In: Automation Science and Engineering (CASE), 2016 IEEE International Conference on, Fort Worth, Texas, pp. 180–187. IEEE (2016)
- [23] Pikul, J., Cohen, I., Shepherd, R.: Stretchable surfaces with programmable texture (2019). US Patent App. 16/161,029
- [24] Pikul, J.H., Li, S., Bai, H., Hanlon, R.T., Cohen, I., Shepherd, R.F.: Stretchable surfaces with programmable 3d texture morphing for synthetic camouflaging skins. *Science* **358**(6360), 210–214 (2017). DOI 10.1126/science.aan5627. URL <https://science.scienmag.org/content/358/6360/210>
- [25] Ringborg, U., Bergqvist, D., Brorsson, B., Cavallin-Ståhl, E., Ceberg, J., Einhorn, N., Frödin, J.e., Järhult, J., Lamnevik, G., Lindholm, C., et al.: The Swedish Council on Technology Assessment in Health Care (SBU) systematic overview of radiotherapy for cancer including a prospective survey of radiotherapy practice in Sweden 2001–Summary and Conclusions. *Acta Oncologica* **42**(5-6), 357–365 (2003)
- [26] Rus, Daniela; Tolley, Michael T.: Design, Fabrication And Control Of Soft Robots. *Nature* pp. 467–475 (2015). DOI 10.1038/nature14543
- [27] Tassa, Y., Erez, T., Todorov, E.: Synthesis and Stabilization of Complex Behaviors through Online Trajectory Optimization. IEEE/RSJ International Conference on Intelligent Robots and Systems (October 2012). DOI 10.1109/IROS.2012.6386025
- [28] Wagner, T.H., Yi, T., Meeks, S.L., Bova, F.J., Brechner, B.L., Chen, Y., Buatti, J.M., Friedman, W.A., Foote, K.D., Bouchet, L.G.: A geometrically based method for automated radiosurgery planning. *International Journal of Radiation Oncology* Biology* Physics* **48**(5), 1599–1611 (2000)
- [29] Wiersma, R.D., Wen, Z., Sadinski, M., Farrey, K., Yenice, K.M.: Development of a frameless stereotactic radiosurgery system based on real-time 6d position monitoring and adaptive head motion compensation. *Physics in Medicine & Biology* **55**(2), 389 (2009)

Olalekan Ogunmolu

Robotics | Control Systems | ML

Rerum Cognoscere Causas: To know the causes of things.

3620 Hamilton Walk
John Morgan Building, #183
Perelman School of Medicine
The University of Pennsylvania
Philadelphia, PA 19104-5156
+1-215-898-5088
ogunmolo@pennmedicine.upenn.edu
scriptedonachip.com

Education

- 2014–2019 **PhD in Electrical and Computer Engineering**, University of Texas at Dallas, Richardson, USA.
"A Multi-DOF Soft Robot Mechanism for Patient Motion Correction and Beam Orientation Selection in Cancer Radiation Therapy." Advisors: Nick Gans (UTD) and Steve Jiang (UT Southwestern Medical Center.) | Committee Members: Drs. Mark Spong, Tyler Summers, Dinesh Bhatia, and Yonas Tadesse. | External Examiner: Prof. Phillip Anderson.
- 2012 **Master of Science in Engineering in Control Systems**, The University of Sheffield, Sheffield, United Kingdom. *"Autonomous Navigation of a Rotorcraft Unmanned Aerial Vehicle using Machine Vision."* Advisor: Tony J. Dodd. | Committee Members: Drs. George Panoutsos and Robin Pursehouse. | Dissertation reviewed by Mahdi Mahfouf.

Publications

Premier IEEE Robotics and Automation Society, Algorithmic Foundations of Robotics, and Medical Physics publications (WAFR, IROS, NIPS, PhysMed, and ICRA) are highly selective venues for archival papers, similar to selective IEEE journals in visibility and strong scientific/engineering communications.

Olalekan Ogunmolu, Xinmin Liu, Nicholas Gans, and Rodney Wiersma, *Mechanism and Constitutive Model of a Continuum Robot for Head and Neck Cancer Radiotherapy*. Submitted to *IEEE International Conference on Robotics and Automation (ICRA 2020)*, September 2019.

Azar Sadeghnejad Barkousaraie, **Olalekan Ogunmolu**, Steve Jiang, and Dan Nguyen. *A Fast Deep Learning Approach for Beam Orientation Selection Using Supervised Learning with Column Generation on IMRT Prostate Cancer Patients*. Accepted at *The International Journal of Medical Physics Research and Practice*, 2019.

Azar Sadeghnejad Barkousaraie, **Olalekan Ogunmolu**, Steve Jiang, and Dan Nguyen. *Using Supervised Learning and Guided Monte Carlo Tree Search for Beam Orientation Optimization in Radiation Therapy*. Appeared in *Artificial Intelligence in Radiation Therapy (AIRT). Lecture Notes in Computer Science, vol 11850. Springer Cham*, 2019.

Olalekan Ogunmolu, Michael Folkerts, Dan Nguyen, Nicholas Gans, and Steve Jiang. *Deep BOO: Automating Beam Orientation Selection in Intensity Modulated Radiation Therapy*. *Algorithmic Foundations of Robotics XIII, International Workshop (WAFR)*, Mérida, Mexico. December 2018.

Olalekan Ogunmolu, Nicholas Gans, and Tyler Summers. *Minimax Iterative Dynamic Game: Application to Nonlinear Robot Control Tasks*. *IEEE/RSJ International Conference on Intelligent Robots and Systems (IROS)*, Madrid, Spain. October 2018. DOI: 10.1109/IROS.2018.8594037.

Olalekan Ogunmolu, Adwait Kulkarni, Yonas Tadesse, Xuejun Gu, Steve Jiang, and Nick Gans. *Soft-NeuroAdapt: A 3-DOF Neuro-Adaptive Pose Correction System For Frameless and Maskless Cancer Radiotherapy*. *IEEE/RSJ International Conference on Intelligent Robots and Systems (IROS)*, Vancouver, BC, Canada. September 2017. DOI: 10.1109/IROS.2017.8206211.

Olalekan Ogunmolu, Nicholas Gans, and Tyler Summers. *Robust Zero-Sum Deep Reinforcement Learning*. *arxiv PrePrints*, arxiv ID:1710.00491, Oct 2017.

Olalekan Ogunmolu, Xuejun Gu, Steve Jiang, and Nicholas Gans. *Nonlinear Systems Identification Using Deep Dynamic Neural Networks*. *arxiv PrePrints*, arxiv ID:1610.01439, Oct 2016.

Olalekan Ogunmolu, Xuejun Gu, Steve Jiang, and Nick Gans. [Vision-based control of a soft-robot for Maskless Cancer Radiotherapy](#). *IEEE Conference on Automation Science and Engineering (CASE)*, Fort-Worth, Texas, August 2016. DOI: 10.1109/CoASE.2016.7743378.

Olalekan Ogunmolu, Xuejun Gu, Steve Jiang, and Nick Gans. [A Real-Time Soft-Robotic Patient Positioning System for Maskless Head-and-Neck Cancer Radiotherapy](#). *IEEE Conference on Automation Science and Engineering (CASE)*, Gothenburg, Sweden, August 2015. DOI: 10.1109/CoASE.2015.7294318.

Azar Sadeghnejad Barkousaraie, **Olalekan Ogunmolu**, Steve Jiang, and Dan Nguyen. [Using supervised learning and guided Monte Carlo tree search for beam orientation optimization in radiation therapy](#). Under review at *International Conference on Medical Image Computing and Computer Assisted Intervention, XXII* (MICCAI), Shenzhen, China. October 2019.

Olalekan Ogunmolu, Dan Nguyen, Xun Jia, Weiguo Lu, Nick Gans, and Steve Jiang. [Automating Beam Orientation Optimization for IMRT Treatment Planning: A Deep Reinforcement Learning Approach](#). *60th Annual Meeting of the American Association of Physicists in Medicine*, Nashville, TN (AAPM). July 2018.

Yara Almubarak, Joshi Aniket, **Olalekan Ogunmolu**, Xuejun Gu, Steve Jiang, Nicholas Gans, and Yonas Tadesse, [Design and Development of Soft Robots for Head and Neck Cancer Radiotherapy](#). *SPIE: Smart Structures + Nondestructive Evaluation*, Denver, CO, U.S.A. March 2018.

Experience

Research

Summer '19 - **Postdoctoral Scholar**, [The University of Pennsylvania](#), Philadelphia, PA, USA.

Present Department of Radiation Oncology, Perelman School of Medicine, University of Pennsylvania.

Summer '19 **Visiting Postdoctoral Scholar**, [The University of Chicago](#), Chicago, IL, USA.

Department of Radiation and Cellular Oncology, Pritzker School of Medicine, The University of Chicago.

Summer '18 **Research Intern**, [Preferred Networks](#), Otemachi, Chiyoda-ku, Tokyo, Japan.

"Preferred Networks is one of a tiny handful of Japanese 'unicorns', or technology startups valued at more than \$1 billion." – The Wall Street Journal, 10/15/2018

Research Intern within the Robotics Team. Worked on stable learning of complex robot motion-planning/manipulation tasks. Implemented Khansari-Zadeh's CLF-DM on the Tokyo Robotics 7-DoF Arm. Proposed a DP approach for better complex robot trajectory imitation.

Fall '17 - **Research Assistant**, Medical Artificial Intelligence and Automation Laboratory, Division of Medical Physics and Engineering, Radiation Oncology Department, UT Southwestern Medical Center.

Research Assistant for Dr. Steve Jiang, Barbara Crittenden Professor of Cancer Research, UTSW Department of Radiation Oncology.

Developed a multidisciplinary approach (spanning Deep learning, optimal control, dynamic programming, and game theory) in order to solve the classic beam orientation optimization (BOO) problem.

Summer - Fall **Research Assistant**, Dr. Tyler Summers, Mechanical Engineering, UT Dallas.

'17 *Dynamic Programming, Decision Theoretic Control, Machine/Reinforcement Learning.*

Developed a conservative controller for mitigating the lack of robustness in multi-stage decision policies.

Fall '14 - **Research Assistant**, Dr. Nick Gans, Electrical Engineering, University of Texas at Dallas.

Spring 19 *Control Systems, Systems Identification, State Estimation and Computer Vision.*

Conceived the prototypical testbed, procured hardware, integrated components to simulate soft robot compensating systems for patients in intensity modulated radiotherapy.

Summer '16 **Hardware Integration Intern**, Amazon Robotics LLC.

SLAM, Software and Hardware Integration Intern.

Helped integrate the hardware and software for the P3-DX robot used as a recreational robot in the Amazon Robotics office.

Spring '16 **Hardware Integration Intern**, Advanced Robotics Lab, Amazon Robotics LLC.

Hardware Integration Intern.

Wrote the codebase for the line scanners used in tracking objects in amazon warehouse assembly lines.

Teaching:

- Now - **Adjunct Instructor, RBOT 250- Robot manipulation, planning and control, Brandeis University.**
Designing course outlines and teaching.
- Fall '14 - '16 **Teaching Assistant, Introduction to Robotics, University of Texas at Dallas.**
Guided students during laboratories in programming the Robai Cyton 300R2 Robot and graded homeworks.
- Spring '15 **Teaching Assistant, Linear Systems (M.S. Class), University of Texas at Dallas.**
Responsible for helping Masters students with linear control theory applications; graded homeworks and midterms.
- Spring '14 **Instructor, Analysis and Design of Digital Systems, Adekunle Ajasin University.**
Developed course modules, sole instructor for sophomore students, graded homeworks, designed and graded exams.
- Summer '14 **Instructor, Digital Logic Design, Adekunle Ajasin University.**
Co-developed course modules, joint-instructor for junior students, graded homeworks, designed and graded exams.

Invited Talks

- Open Robotics [Soft-Robotic Position Correction Mechanisms in Intensity-Modulated Radiation Therapy.](#)
[Open Robotics Foundation](#), Mountain View, CA, USA. January 2019.
- Stanford University [Robotic Radiotherapy: Automating Position Correction in Intensity-Modulated Radiation Therapy.](#)
Department of Energy Resources Engineering, **Stanford University**, Stanford, CA, USA. November 2018.
- UChicago [Robotic Radiotherapy: Automating Position Correction in Intensity-Modulated Radiation Therapy.](#)
Department of Radiation and Cellular Oncology, **The University of Chicago**, Chicago, IL, USA. November 2018.
- ATR CNS Labs [Minimax Iterative Dynamic Game.](#)
Department of Brain Robot Interface, **Computational Neuroscience Labs, ATR**, Osaka, Japan. August 2018.
- Preferred Networks [Neural Networks and Adaptive Control.](#)
[Preferred Networks Tech. Talk](#), Chiyoda-ku, Tokyo. Japan. August 2018.
- Google [SoftNeuroAdapt: A 3-DoF Neuro-Adaptive Healthcare System.](#)
Work presented by Nick Gans, Google Robotics, Mountain View, CA. USA. September 2017.
- UTARI, Fort Worth, TX [A Wearable Soft Robotic Modular System for Head and Neck Motion Correction in Intensity-Modulated Radiation Therapy.](#)
University of Texas at Arlington Research Institute, Fort Worth, Texas, USA. May 2019.
- EFSC'17 Vancouver, BC [Soft Robotic Modules as Position Correcting Mechanisms in Cancer RT.](#)
3rd Entrepreneurship Forum & Start-up Competition, EFSC'17, Vancouver, BC, Canada. September 2017.
- UTSW, Dallas, TX [A 3-DOF Neuro-Adaptive Patient Pose Correcting System For Frameless and Maskless Cancer Radiotherapy.](#)
Physics Research Seminar Series, Radiation Oncology Department, UT Southwestern Medical Center, Dallas, TX, USA. March 2017.
- IEEE Arlington, TX [Towards automated accurate patient positioning in maskless cancer radiotherapy.](#)
IEEE Computational Intelligence Society, UT Arlington, TX, USA. December 2015.

Awards and honors

- **Google AI Travel and Conference Grant** October 2018
- **IEEE RAS/IROS Travel Award (IROS 2018)** August 2018
- Finalist at the [3rd Entrepreneurship Forum and Startup Competition](#) Sponsored by IEEE Robotics and Automation Society, KUKA AG, and Univ. Hamburg August 2017
- **NSF Doctoral Consortium Award (IROS 2017)** August 2017
- **Mary and Richard Templeton Graduate Fellowship** August 2017
- **ROSCon Scholarship** (Open Software for Robotics Foundation) July 2017
- President's **Teaching Excellence Award** for Teaching Assistants Nom. Feb. 2017

○ Golden Key International Honour Society	Inducted Dec. 2016
○ IEEE RAS/ISAM Travel Award (CASE 2016)	August 2016
○ Ericsson Graduate Fellowship	2015 - 2016
○ Jonsson Scholarship	2014 - 2015
○ Achievement Award, University of Florida (Declined)	Fall 2014
○ PTDF Overseas Scholarship Award, £25,500+ for one year. (~1.7% acceptance)	2011
○ Federal Government (of Nigeria) Scholarship (~3.6% acceptance)	2002
○ Ondo State (Nigeria) Scholarship (~10% acceptance)	2004

Select Leadership

Peer Reviewing Activities (Research)

- 2019-Present **JBHI**, *An IEEE Journal of Biomedical and Health Informatics Access*.
- 2019-Present **External Grants Reviewer**, *AI for Species Discovery*, [National Geographic Society](#).
- 2018-Present **Automatica**, *The International Federation of Automatic Control (IFAC)*, Impact Factor: 6.355.
- 2017-Present **Access**, *IEEE Access Journal*.
- 2017-Present **NCAA**, *Springer's Neural Computing and Applications*, Impact Factor: 4.664.
- 2018-Present **CDC**, *IEEE International Conference on Decision and Control*, Flagship Control and Decision-Making Control Conference Proceedings in the World, Impact Factor: 4.09, H-index: 42.
- 2017-Present **DSCC**, *American Society of Mechanical Engineers (ASME) Dynamic Systems and Control Conference*, Conference Proceedings, H-index: 8.
- 2017-Present **ICRA**, *IEEE International Conference on Robotics and Automation*, Flagship IEEE Robotics and Automation Society Conference in the World, H5-index: 82.
- 2017-Present **IROS**, *IEEE/Robotics Society of Japan (RSJ) International Conference on Intelligent Robots and Systems*, Flagship IEEE/RSJ Conference on Robotics, H5-index: 58.
- 2017-Present **ACC**, *IEEE American Control Conference*, Premiere American Control Conference Venue, H5-index: 41.
- 2017-Present **The IFAC World Congress**, *The International Federation of Automatic Control*, A worldwide, interdisciplinary congress of scientists and engineers to share up-to-date, complete and universal view of control and analysis techniques, Impact Factor: 2.653 at 2014.

Miscellaneous

- 2017 **Invited Contributor**, *IEEE/RSJ International Conference on Robots and Intelligent Systems (IROS)*, Abstract Only Track, Vancouver, BC, Canada.
- 2017 – Now **Member, IEEE Robotics and Automation Society**.
- 2016–Now **Member, IEEE Boston**, Greater Boston, USA.
- 2015 – 2016 **Science instructor**, *IEEE Dallas Shoulder of Giants Workshops*, Dallas, TX.
Participant at IEEE Dallas Young Professionals community outreaches in promoting STEM education and awareness in the Dallas/Fort-Worth Metroplex.
- 2015 **Summer Science Program**, *University of Texas at Dallas*, Richardson, TX.
Trained high-school kids in basic robots control and programming with the Berkeley Snap! kit and arduino.
- 2012 **Workshop participant**, *ILA Berlin Airshow*, Berlin, Germany.
Selected by Cassidian (an EADS company) for the *Aerospace Systems Engineering* workshop.
- 2012 **Workshop participant**, *Farnborough International Airshow*, NE Hampshire, England.
Selected by Airbus (an EADS company) among participants at the *UAV and Fighter Aircraft* workshop.

Mentoring

Undergraduate mentoring:

- Summer 2017 Rachael Thompson. Plano High School Student. Currently an undergrad at MIT's CSAIL. Class of 2021
- 2013-2014 Blessing K. Currently a PhD student at Tufts University.

2016 - 2017 Alex Tomkovich. Computer Engineering Junior.

Spring 2015 Grant Carr. Computer Engineering Junior.

Masters mentoring:

2016 – 2017 Adwait Kulkarni. Mechanical Engineering Masters student (Currently at Drov Technologies, MN).

2015 Ajith Venkateswaran. Computer Engineering Masters student (Currently Senior Robotics Software Engineer, Samsung Research, America).

Computing

OS OSX, Debian, Windows.

Programming C++, Python, Mathematica, MATLAB, LabVIEW.

CAD Adobe Illustrator, Blender.

ROS Hydro, Indigo, Jade, Kinetic, and Melodic, Bouncy Bolson distros.

Libraries Point Cloud Library, OpenCV, Torch7, Eigen, Docker, PyTorch, OpenAI Gym, MuJoCo, Numpy, SciPy, Scikit-Learn, C++11/14 standards.

Web HTML, Markdown, node.js.

Languages

English Reads, writes, and speaks fluently

Lived in Nigeria, United Kingdom and United States.

Japanese Basic proficiency

Lived in Japan for 3 months.

Yoruba Reads, writes, and speaks fluently.

Native Nigerian Language. Spoken at home.

Last updated: November 24, 2019

Soft-NeuroAdapt: A 3-DOF Neuro-Adaptive Patient Pose Correction System For Frameless and Maskless Cancer Radiotherapy

Olalekan Ogunmolu¹, Adwait Kulkarni², Yonas Tadesse², Xuejun Gu³, Steve Jiang³, and Nicholas Gans¹

Abstract— Precise patient positioning is fundamental to successful removal of malignant tumors during treatment of head and neck cancers. Errors in patient positioning have been known to damage critical organs and cause complications. To better address issues of patient positioning and motion, we introduce a 3-DOF neuro-adaptive soft-robot, called Soft-NeuroAdapt to correct deviations along 3 axes. The robot consists of inflatable air bladders that adaptively control head deviations from target while ensuring patient safety and comfort. The adaptive-neuro controller combines a state feedback component, a feedforward regulator, and a neural network that ensures correct adaptation. States are measured by a 3D vision system. We validate Soft-NeuroAdapt on a 3D printed head-and-neck dummy, and demonstrate that the controller provides adaptive actuation that compensates for intrafractional deviations in patient positioning.

I. INTRODUCTION

Radiation-based treatment of head and neck (H&N) cancers often involve intensity-modulated radiotherapy (IMRT), which modulate radiation dosage and shaping of treatment beam to the precise size of tumor cells. IMRT carefully targets organs, while minimizing toxicity and exposure of organs at risk. Used alongside image guided radiotherapy (IGRT), IMRT assures precision of dosage targets: a patient is positioned on a treatment table after dosage planning by a physician, then a rigid robotic couch is used for motion alignment during surgery. While conventional RT uses rigid immobilization techniques such as masks, frames, arm positioning devices or vacuum mattresses [1], IGRT methods employ ultrasound, 3D imaging systems, 2D X-ray devices and/or computed tomography to instantly amend positioning errors, and improve daily radiotherapy fractions' precision.

Precise, and repeatable patient positioning is therefore crucial in RT treatments when escalation of dose is necessary in a target volume and exposure of adjacent organs is to be minimized. Because it does not require rigid masks and body fixators, IGRT is more comfortable for the patient as well as more accurate with the aid of highly accurate localization

*This work was supported by the Radiation Oncology Department, UT Southwestern, Dallas, Texas, USA

¹Olalekan Ogunmolu and Nicholas Gans are with the Department of Electrical Engineering, University of Texas at Dallas, Richardson, TX 75080, USA {olalekan.ogunmolu, ngans}@utdallas.edu

²Adwait Kulkarni and Yonas Tadesse are with the Department of Mechanical Engineering, University of Texas at Dallas, Richardson, TX 75080, USA {axf151530, ytt110030}@utdallas.edu

³Xuejun Gu and Steve Jiang are with the Department of Radiation Oncology, University of Texas Southwestern Medical Center, Dallas TX 75390, USA {Xuejun.Gu, Steve.Jiang}@utsouthwestern.edu

systems. Sterzing [2], after an extensive review of IGRT methods, found IGRT to be more precise and safer than conventional radiotherapy. But setup errors (interfractional) or patient motion (intrafractional) errors often need to be accounted for during RT. While intrafractional errors can be minimized by highlighting the importance of voluntary stillness to the patient, suitable means of immobilization and adaptive positioning are necessary when the patient moves involuntarily or sleeps. This would assure precise and accurate targeting of critical organs while keeping the patient comfortable during treatment. Frameless and Maskless (F&M) IGRT is promising because it minimizes invasiveness and reduces setup times while comfortably positioning the patient.

We present **Soft-NeuroAdapt**, a set of three **soft** actuators that employ a **neuro**-controller to **adaptively** compensate for positioning deviations. Soft robot systems are elastomeric active and reactive nonlinear compliant systems, suitable to the task of human-machine interaction. They can dynamically change their stiffness and activate their surfaces to provide a desired motion on a human body part. Their characteristic morphological computation properties [3] make them suitable for autonomous control including inflation, deflation and reaching. Exhibiting highly nonlinear dynamics, controlling them for precise actuation is complicated. While a metric-based modeling approach may work in highly-structured environments, system parameters and dynamics change with different patients' head and upper torso anatomy such that achieving precise control is best achieved with a learning-based method. But reliable high parameter-space adaptive-control methods rely on open-loop adaptation mechanisms based on extensive design techniques. Our goal is to derive a learning-based controller, going beyond task-specific, expert-driven methods in order to adaptively generalize to new control systems.

Following our recent investigative studies, [4], [5], on 1-DoF soft-robot compensation systems, we present a 3-DoF soft robot system that addresses 3-DoF involuntary intrafractional motions of the head and neck (H&N) region during F&M RT. This work presents a neuro-dynamics estimator that learns the underlying system model, then adapts to the model in its control law to provide bounded tracking of set trajectory. The controller corrects intrafractional (involuntary) patient motions along three defined axes namely head pitch, roll and elevation angles for a patient lying in a supine position on a table. We use three inflatable air bladders (IABs), actuated through a system of inlet and outlet solenoid proportional valves. The controller uses state

feedback to provide bounded stability of states, a reference trajectory component to provide command tracking and a neural-network component to adaptively converge states that start outside of the sphere of stability into the region of stability. We perform head pose tracking in the 3D space of a stereo-camera, and we conduct experiments to validate the proposed bio-pneumatic system and controller.

This paper is organized as follows: section II presents related work, section III describes the hardware setup, section IV describes the vision segmentation algorithm and 3-DOF pose estimation, while section V describes the adaptive-neuro control algorithm. We discuss experiments in VI and provide discussions and future work in VII.

II. RELATED WORK

Studies on the feasibility of non-rigid immobilization devices during cranial stereotactic radiosurgery (SRS) fall largely under *inspection-based* non-rigid immobilization devices, and *correction-based* non-rigid immobilization systems.

Inspection-based Systems: In [6], Cervino et al. used expandable foams that fit a patient's head while leaving the face opened. Patient set-up was performed using computed tomographic (CT) scans before treatment. They found an average treatment time of 26 minutes with patients who slept during experiments taking longer as a result of involuntary movements. In [7], the authors evaluated the accuracy of a head mold that minimally immobilized a patient's H&N region while leaving the face free in a controlled positioning experiment with volunteers. 3D surface reconstruction imaging system was used in monitoring patients' position so that treatment was stopped whenever motion exceeded a defined threshold. While the monitoring system showed great clinical accuracy, it required high patient cooperation to achieve immobilization. Using a head mold, an open face-mask, and a mouthpiece, Li et al. [8] quantified the residual rotation and positioning errors in an open-loop setting to ascertain the reduction in setup time during patient positioning setup. They reported the head mold and open face mask system could restrict head motions to within $0.6^\circ \pm 0.3^\circ$ with the time spent on in-situ motion corrections limited to 2.7 ± 1.0 min.

Correction-based Systems: In [9], a 4-DOF motion correction system was used in a real-time motion compensation of a phantom and in human trials. An optical sensing system tracked the pose of the head and a decoupling control law regulated the xyz -translational and pitch motions of the head. They reported target accuracy of 0.5mm and 0.2° with the decoupling controller for each axis of the 4-DOF motion. The system relied on stepper motor actuators and other electro-mechanical (EM) components positioned under the patient's H&N region. These devices have the undesirable effect of attenuating treatment beams during RT, and as a result are not recommended during clinical procedure. The presence of the EM stages can significantly reduce the efficiency of the incident radiation targeted to tumor cells.

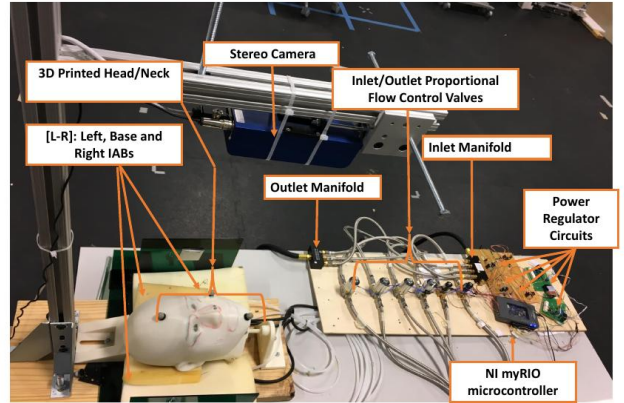


Fig. 1: Hardware Description

To address these concerns, we proposed soft-robot actuators for H&N motion compensation during F&M cancer radio-therapy [4], [5] actuated by pneumatic valves which are kept away from the head. Plastic hoses and silicone connectors convey air into and out of the soft robots that laid beneath the head so that our motion correction system does not interfere with planned dosage from the treatment beam. In our evaluations, we used pneumatic valves mounted on a movable plywood and connect these to the soft robots with long silicone tubes so that the medical physicist can separate EM components from the patient as deemed necessary during treatment. While our previous works related to controlling the 1-DoF motion of the head along the z-axis, here we address the 3-DOF control of the head using a surface reconstructing sensor and control the pose of the head to follow set trajectories in real-time.

III. HARDWARE DESIGN OVERVIEW

The actuation mechanism consists of three custom-designed inflatable air bladders (IABs) made from elastomeric polymers. The base IAB (beneath the head's posterior) is 180mmx280mm when flat and inflates to a maximum width of ~ 75 mm while the other two are 180mmx140mm in size. The IABs consist of inflatable rubber encased in a breathable foam pad for comfort, modified to be the size of an average adult male; they have separate inlet and outlets openings, connected with crack-resistant polyethylene tubing (1/8" ID and 1/4" OD); this sustains pressure of up to 320psi.

Each hose leads to a proportional solenoid valve, which is in turn connected to rectangular manifolds (one manifold to the inlet supply and the second to the outlet supply). We use six Dakota Instruments EM valves (Model PSV0105, Orangeburg, NY, USA) to supply proportional torques to the soft actuators. A regulated air canister supplied constant air pressure at 15psi to the inlet-air conveying manifold, while a suction pump supplied vacuum pressure at 12 psi to the valves that removed air from the bladders. The air rate of flow into or out of each bladder was controlled via custom-built voltage regulating circuits which got PWM signals from a National Instruments (NI) myRIO microcontroller. We 3D printed a custom manikin head, measuring $155 \times 240 \times 200$

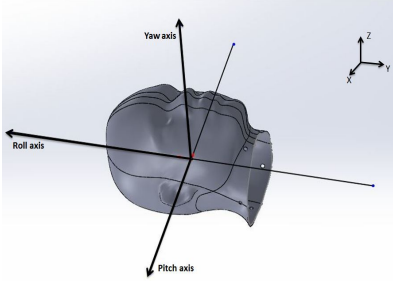


Fig. 2: Head Coordinate System

mm ($W \times L \times D$) and comparing between 50% and 75% weight of a typical adult male head or 99% of a typical adult female head; it weights 5kg – above average and reasonable. The head was fitted with a ball-joint in the neck to replicate motion of the human head about the neck. An Ensenso 3D camera is mounted near 45° above the head to measure the pose of the head in real time. All vision processing, systems modeling and control laws were computed on a CORSAIR PC. We exchange the neuro-control and sensor signals via the publish-subscribe IPC of the ROS middleware installed on the PC. Adaptive control laws were sent via udp packets to the RIO microcontroller. The system setup is shown in Fig. 1.

The reference frame of the head is described as follows: the pitch/x-axes points from the left ear out of the right ear, the yaw/z-axes points from the back of the head through the forehead through, and the roll/y-axes goes from the neck through the top of the head. The left and right bladders control the roll angles/x-axes motions while the bladder underneath the head, henceforth referred to as the base bladder, controls the pitch angles and z-axis motions. The reference frame is illustrated in Fig. 2.

IV. VISION-BASED POSE ESTIMATION

The model head lies in a supine position above a planar table as shown in Fig. 1. We employed a 3D camera from Ensenso GmbH (model N35) to reconstruct the surface image and measure head pose. The N35 camera captures multiple image pairs during exposure; each image pair is made up of different patterns, controlled by piezo-actuators. A stereomatching algorithm gathers the information from all image pairs after capture to produce a high-resolution point cloud (PCL) of the scene [10]. We mounted the 3D sensor such that its lens faced the head at approximately 45° from the vertical during experiments. Our goal is to control the motion of the head about three axes, namely z , pitch and roll axes as described in section III; this section presents how we go about extracting representable features from the face.

A. Face Segmentation

The dense point cloud of the scene has (i) marked jump in rendered points along the z -axis of the camera; this is because of the single view angle by the camera; (ii) the scene clutter and lack of multiple camera view angles does not affect the representation of the face; (iii) thus, through spatial decomposition of the scene, we can separate the face

from the scene. However, the point cloud is computed from monochromatic IR image pairs (with no texture information) making morphological operations difficult; due to the multiple image pairs used in 3D reconstruction to generate a highly accurate measurement, the camera is limited to a maximum frame rate of 10Hz. Inspired by Rusu's work [11], we divide the segmentation problem into stages, with each stage involving segmenting out candidates that do not belong to the object we want to identify (the frontal face) in the scene. Our engineering philosophy in the segmentation phase is inspired by spatial decomposition methods that determine subdivisions and boundaries to allow retrieval of data that we want given a measure of proximity. In this case, we know that the location of the table cannot exceed a given height during experiments and the camera's position is fixed while the head moves based on bladders' actuation. Separating objects that represent planar 2D geometric shapes from the scene therefore simplifies the face segmentation algorithm. By finding and removing objects that fit primitive geometric shapes from the scene, clustering of the remaining objects would yield the face of the patient in the scene. We fit a simplified 2D planar object to the scene such that searching for points $\mathbf{p}_i \in \mathcal{P}$ that support a 2D plane can be found within a tolerance defined by the inequality $0 \leq |d| \leq |d_{max}|$, where $|d_{max}|$ represents a user-defined threshold to segment out [11].

We proceed as follows:

- The point cloud of the scene was acquired from the computed disparity map of the two raw camera images;
- To minimize sensor noise whilst preserving 3D representation, the acquired point cloud was downsampled using a SAmple Consensus (SAC)-based robust moving least squares algorithm (RMLS) [11, §6];
- We then searched for the edges of 2D planar regions in the scene with Maximum Likelihood SAmple Consensus (MLESAC) [12], and we bound the resulting plane indices by computing their 2D convex hull;
- A model fitting stage extrudes the computed hull (of objects lying above the 2D planar region) into a prism model based on a defined L_1 Manhattan distance; this gives the points whose height threshold is about the region of the face in the scene [13];
- We then cluster the remaining points based on a heuristically determined L_2 distance between points remaining within the polygonal plane. The largest cluster gives us the face.

The result of the resampling algorithm is shown in the top-right image of Fig. 3.

To simplify the complexity of the planar structure in the scene, the table is modeled as a 2D planar geometric primitive so that finding points that fit a defined model hypothesis involves estimating a single distance to the frontal plane of the table surface rather than multiple points if the model was represented with points. Searching for horizontal planes that are perpendicular to the z -axis of the head is carried out using the maximum likelihood SAC [12] algorithm implemented

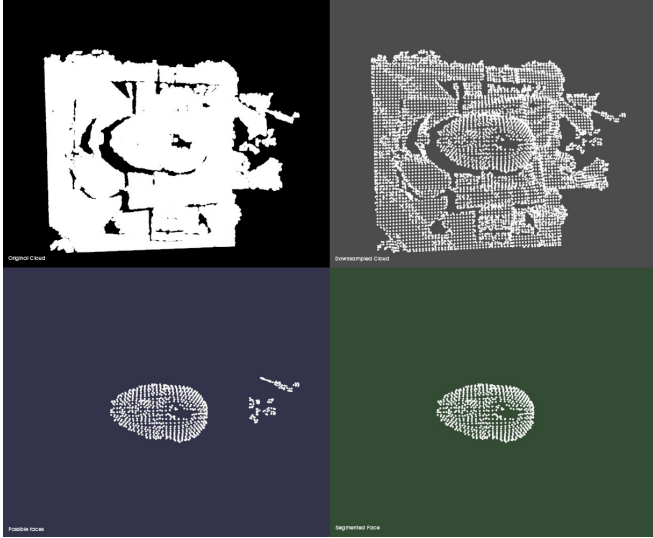


Fig. 3: [Top-left]: Dense point cloud of the experimental setup scene. [Top right]: Downsampled cluttered cloud of the left scene. [Bottom-left]: Using RANSAC, we searched for 2D plane candidates in the scene and compute the convex hull of found planar regions. We then extrude point indices within the hull into a prismatic polygonal model to give the face region. [Bottom-right]: An additional step clusters the resultant cloud based on a Euclidean distance. The largest cluster is taken to be the face.

TABLE I: Plane Segmentation Algorithm

-
1. **for** $i = 1$ to N **do**
 2. sample non-collinear points $\{p_i, p_j, p_k\}$ from \mathcal{P}
 3. calculate the model coefficients $ax + by + cz = d$
 4. find distances from all $\mathbf{p} \in \mathcal{P}$ to the plane (a, b, c, d)
 5. store points $\mathbf{p}^* \in \mathcal{P}$ that satisfy the model hypothesis, $0 \leq |d| \leq |d_{max}|$.
 6. **return** maximum of the stored points \mathbf{p}^* .

in the PCL Library [14] to generate model hypotheses. The plane segmentation algorithm is defined in Table I.

The plane segmentation process is run once. Once the plane model is found, its indices and those of objects lying above it are separated and stored in separate data structures. Every subsequent iteration consists of (i) computing the 2D convex hull of point indices of objects above the table using the *Qhull* library¹, (ii) using a pre-defined prismatic model candidate to hold extruded points to the approximate facial height above the table; and (iii) separating the face from every other point in the resulting cloud through the Euclidean clustering (EC) method of [15]. A distinct point cluster is defined if the points in cluster $C_i = \{\mathbf{p}_i \in \mathcal{P}\}$ and cluster $C_j = \{\mathbf{p}_j \in \mathcal{P}\}$ satisfy the L_2 -distance threshold

$$x \leq \min \|\mathbf{p}_i - \mathbf{p}_j\|_2$$

Finding the face in the scene after carrying out EC algorithm is a question of finding the largest index in the list \mathcal{C} . This takes $O(n)$ (linear) time for n clusters. The face segmentation results are presented in Fig. 3. We then compute the Cartesian position of the face with respect to the

camera origin by taking the center of mass of the segmented facial region (bottom-right image of Fig. 3). This is obtained by calculating the mean-value of all the points in the resulting cloud (≈ 600 points on average).

B. Head Pose Estimation

With the facial point cloud segmented, we define three points on the head. Our goal is to compute the optimal translation and rotation of the head from a model point set $\mathbf{X} = \{\vec{x}_i\}$ to a measured point set $\mathbf{P} = \{\vec{p}_i\}$, where $N_x = N_p = 3$, and the point $\vec{x}_i \in \mathbf{X}$ has the same index as $\vec{p}_i \in \mathbf{P}$. Following the approach of Besl and McKay in [16], we compute the cross-covariance matrix of \mathbf{P} and \mathbf{X} as Σ_{px} , extract the cyclic components of this skew symmetric matrix as Δ , and use it to form the symmetric 4×4 matrix $\mathbf{Q}(\Sigma_{px})$ as follows,

$$\mathbf{Q}(\Sigma_{px}) = \begin{bmatrix} \text{tr}(\Sigma_{px}) & \Delta^T \\ \Delta & \Sigma_{px} + \Sigma_{px}^T - \text{tr}(\Sigma_{px})\mathbf{I}_3 \end{bmatrix}. \quad (1)$$

The unit eigenvector, q_R , that corresponds to the maximum eigenvalue of $\mathbf{Q}(\Sigma_{px})$ is selected as the optimal rotation quaternion; we find the optimal translation vector as

$$\vec{q}_T = \vec{\mu}_x - \mathbf{R}(\vec{q}_R)\vec{\mu}_p \quad (2)$$

where μ_x and μ_p are the mean of point sets \mathbf{X} and \mathbf{P} respectively. Obtaining the roll, pitch and yaw angles from q_R is trivial and the pose of the face is described by tuples $[q_T, q_R] = \{x, y, z, \theta, \phi, \psi\}$ with respect to the world frame. Given the 3-DOF setup, we choose to control three states of the head: z, θ, ϕ (i.e. z , roll, and pitch).

V. CONTROL DESIGN

Our control philosophy is governed by the state feedback and feedforward regulation problem, with an adaptation mechanism based off an estimation of the head pose given a priori information about the systems states and past control actions. We propose an adaptive control strategy in a Bayesian setting, which given an initial prior distribution of controls and 3-DOF head pose, minimizes a cost criterion as the expected value of control laws that will yield a future desired head pose. We consider the pwm voltages that power the valves as input, \mathbf{u} , the head pose as the output, \mathbf{y} and an unknown disturbance $\mathbf{w}(k)$. We first describe the nonlinear function approximator model $\hat{f}(\mathbf{u}(k-d), \mathbf{y}(k), \mathbf{w}(k))$, which is constructed from memory-based input and output experimental data that satisfy

$$\begin{aligned} Z^N = \{u(k), u(k-1), \dots, u(k-n_u), \\ y(k), y(k-1), \dots, y(k-n_y)\} \end{aligned} \quad (3)$$

that satisfy the Lipschitz continuity. (3) implies an input $\mathbf{u}(\cdot)$ at time $k-d$, produces an output $\mathbf{y}(k)$ at d time instants later. The next section describes how we formulate the class of minimum error variance controllers that predict the effect of actions $\mathbf{u}(\cdot)$ on states $\mathbf{y}(\cdot)$ using a self-tuning regulator.

¹The Qhull library: <http://www.qhull.org/>

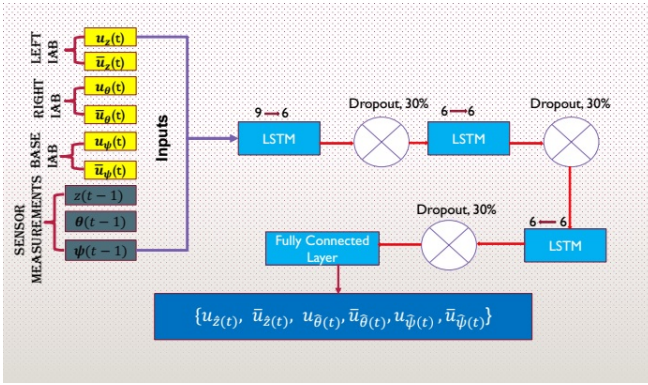


Fig. 4: Function Approximator Model

A. Adaptive Neuro-Control Formulation

Following our previous approach in [5, §IV.B], we fix a persistently exciting input signal $u_{ex} \in L_2 \cap L_\infty$ to excite the nonlinear modes of the system. We then parameterized the system with a neural network with sufficient number of neurons. The neural network (NN) provided information on the changing parameters of the system during control trials. The adjustment mechanism is computed from inverse Lyapunov analysis, where we choose adaptive laws that guarantee a nonpositive-definite Lyapunov function candidate when evaluated along the trajectories of the error dynamics.

Our contribution is the approximation of the nonlinear system by a long short-term memory (LSTM) [17], equipped with an adequate number of neurons in its hidden layers. We parameterized the last layer of the network with a fully connected layer that outputs control torques to the valves. The neural network can be seen as a memory-based model that remembers effective controls for the adaptation mechanism in the presence of uncertainties and external disturbance.

The neural network is shown in Fig. 4. Depending on the region of attraction of the system the network is approximating, it parameterizes the nonlinear dynamical system $f(\cdot)$ and maps the parameterized model to appropriate valve torques. There exists additional feedforward + feedback terms in the global controller (introduced shortly) that guarantee system stability and robustness to uncertainties. Therefore, the global controller keeps the states of the system bounded under closed-loop dynamics, ensures convergence to desired trajectories from states that are initialized outside the domain of attraction, and guarantees robust reference tracking in the presence of non-parametric uncertainties.

For the multi-input, multi-output (MIMO) adjustable system,

$$\dot{\mathbf{y}} = \mathbf{A}\mathbf{y} + \mathbf{B}\Lambda(\mathbf{u} - f(\mathbf{y}, \mathbf{u})) + \mathbf{w}(k) \quad (4)$$

where $\mathbf{y} \in R^n$, $\mathbf{u} \in R^m$ are known input and output vectors, and $\mathbf{A} \in R^{n \times n}$, $\Lambda \in R^{m \times m}$ are unknown matrices, $\mathbf{B} \in R^{n \times m}$, $sgn(\Lambda)$ are known matrices, and $\mathbf{w}(k) \in R^n$ is a bounded time-varying unknown disturbance, upper-bounded by a fixed positive scalar \mathbf{w}_{max} . We make the following

assumptions:

- a dynamic RNN with N neurons, $\varphi(\mathbf{y})$, exists that will map from a compact input space $\mathbb{U} \supset \mathbf{u}$ to an output space $\mathbf{y} \subset \mathbb{Y}$ on the Lebesgue integrable functions with closed interval $[0, T]$ or open-ended interval $[0, \infty)$;
- the nonlinear function $f(\cdot)$ is exactly $\Theta^T \Phi(\mathbf{y})$ with vectorized coefficients $\Theta \in R^{N \times m}$ and a Lipschitz-continuous vector of basis functions $\Phi(\mathbf{y}) \in R^N$;
- inside a ball \mathbf{B}_R of known, finite radius R , the ideal NN approximation $f(\mathbf{y}) : R^n \rightarrow R^m$, is realized to a sufficient degree of accuracy, $\varepsilon_f > 0$;
- the process noise $\mathbf{w}(k)$ is estimated alongside model parameters by the dynamic RNN;
- outside \mathbf{B}_R , the NN approximation error can be upper-bounded by a known scalar function ε_{max} such that $\|\varepsilon\| \leq \varepsilon_{max}$, $\forall \mathbf{y} \in \mathbf{B}_R$;
- there exists an exponentially stable reference model

$$\dot{\mathbf{y}}_m = \mathbf{A}_m \mathbf{y}_m + \mathbf{B}_m \mathbf{r}, \quad (5)$$

with a Hurwitz matrix $\mathbf{A}_m \in R^{n \times n}$ and $\mathbf{B}_m \in R^{n \times m}$ commanded by a reference signal $\mathbf{r} \in R^m$. For this system, we note that $n = 3$ and $m = 6$. Our objective is to design an model-reference adaptive controller (MRAC) capable of operating in the presence of parametric (ε_f), and non-parametric ($\mathbf{w}(k)$) uncertainties so as to assure the boundedness of all signals within the closed-loop system. We propose the following controller

$$\dot{\mathbf{y}} = \hat{\mathbf{K}}_y^T \mathbf{y} + \hat{\mathbf{K}}_r^T \mathbf{r} + \hat{f}(\mathbf{y}, \mathbf{u}), \quad (6)$$

where $\hat{\mathbf{K}}_y$ and $\hat{\mathbf{K}}_r$ are adaptive gains to be designed shortly. The $\hat{\mathbf{K}}_y^T \mathbf{y}$ term keeps the states of the approximation set $\mathbf{y} \in \mathbf{B}_R$ stable, while the $\hat{\mathbf{K}}_r^T \mathbf{r}$ term causes the states to follow a given reference trajectory. The function approximator $\hat{f}(\cdot)$ ensures states that start outside the approximation set $\mathbf{y} \in \mathbf{B}_R$ converge to \mathbf{B}_R in finite time (it converges non-parametric errors ε_f that puts certain states out of the approximation set into \mathbf{B}_R). We can generally write the NN model as

$$\hat{f}(\mathbf{y}) = \hat{\Theta}^T \Phi(\mathbf{y}) + \varepsilon_f,$$

where $\hat{\Theta}^T$ denotes the vectorized weights of the neural network and $\Phi(\mathbf{y})$ denotes the vector of inputs and outputs defined as

$$\Phi(\mathbf{y}) = \{\mathbf{y}(k-d) \cdots \mathbf{y}(k-4), \mathbf{u}(k-d) \cdots \mathbf{u}(k-d-5)\}, \quad (7)$$

and ε_f is the approximation error. The closed-loop dynamics therefore become

$$\dot{\mathbf{y}} = \mathbf{A}\mathbf{y} + \mathbf{B}\Lambda \left(\hat{\mathbf{K}}_y^T \mathbf{y} + \hat{\mathbf{K}}_r^T \mathbf{r} + \hat{f}(\cdot) - f(\cdot) \right). \quad (8)$$

We assume nonlinear function and approximator matching conditions, $f(\cdot) = \hat{f}(\cdot)$, such that after rearrangement, (8) can be written as

$$\dot{\mathbf{y}} = (\mathbf{A} + \mathbf{B}\Lambda \hat{\mathbf{K}}_y^T) \mathbf{y} + \mathbf{B}\Lambda (\hat{\mathbf{K}}_r^T \mathbf{r} + \varepsilon_f). \quad (9)$$

Furthermore, we assume model matching conditions with

ideal constant gains \mathbf{K}_y and \mathbf{K}_r so that

$$\mathbf{A} + \mathbf{B}\Lambda\hat{\mathbf{K}}_y^T = \mathbf{A}_m, \quad \text{and} \quad \mathbf{B}\Lambda\hat{\mathbf{K}}_r^T = \mathbf{B}_m, \quad (10)$$

from which

$$\begin{aligned} \mathbf{A} + \mathbf{B}\Lambda\hat{\mathbf{K}}_y^T - \mathbf{A}_m &= \mathbf{B}\Lambda\tilde{\mathbf{K}}_y^T \quad \text{and} \\ \mathbf{B}\Lambda\hat{\mathbf{K}}_r^T - \mathbf{B}_m &= \mathbf{B}\Lambda\tilde{\mathbf{K}}_r^T, \end{aligned} \quad (11)$$

where $\tilde{\mathbf{K}}_y^T = \mathbf{K}_y^T - \hat{\mathbf{K}}_y^T$ and $\tilde{\mathbf{K}}_r^T = \mathbf{K}_r^T - \hat{\mathbf{K}}_r^T$. The generalized error state vector $\mathbf{e}(k) = \mathbf{y}(k) - \mathbf{y}_m(k)$ has dynamics $\dot{\mathbf{e}}(k) = \dot{\mathbf{y}}(k) - \dot{\mathbf{y}}_m(k)$, so that by substituting (5) and (8) into $\dot{\mathbf{e}}$, we have

$$\dot{\mathbf{e}}(k) = \mathbf{A}_m\mathbf{e}(k) + \mathbf{B}\Lambda[\tilde{\mathbf{K}}_r^T \mathbf{r} + \tilde{\mathbf{K}}_y^T \mathbf{y} - \varepsilon_f] \quad (12)$$

The estimation error will be bounded as long as $\mathbf{y} \in \mathbf{B}_R$. Our goal is to keep $\mathbf{y} \in \mathbf{B}_R$.

Theorem: Given correct choice of adaptive gains $\hat{\mathbf{K}}_y$ and $\hat{\mathbf{K}}_r$, the error vector $\mathbf{e}(k)$, with closed loop time derivative given by (12) will be uniformly ultimately bounded, and the state \mathbf{y} will converge to a neighborhood of \mathbf{r} .

Proof: We choose a Lyapunov function candidate \mathbf{V} in terms of the generalized error state space \mathbf{e} , gains, $\tilde{\mathbf{K}}_y^T$, $\tilde{\mathbf{K}}_r^T$, and parameter error $\varepsilon_f(\mathbf{y}(k))$ space ([18], [19], [20]) as follows

$$\begin{aligned} \mathbf{V}(\mathbf{e}, \tilde{\mathbf{K}}_y, \tilde{\mathbf{K}}_r) &= \mathbf{e}^T \mathbf{P} \mathbf{e} + \text{tr}(\tilde{\mathbf{K}}_y^T \Gamma_y^{-1} \tilde{\mathbf{K}}_y |\Lambda|) \\ &\quad + \text{tr}(\tilde{\mathbf{K}}_r^T \Gamma_r^{-1} \tilde{\mathbf{K}}_r |\Lambda|) \end{aligned} \quad (13)$$

where Γ_y and Γ_r are fixed symmetric, positive definite (SPD) matrices of adaptation rates, $\text{tr}(\mathbf{A})$ denote the trace of matrix \mathbf{A} and \mathbf{P} is a unique SPD matrix solution of the algebraic Lyapunov function

$$\mathbf{P}\mathbf{A}_m + \mathbf{A}_m^T \mathbf{P} = -\mathbf{Q}, \quad (14)$$

where \mathbf{Q} is a SPD matrix. Take the time derivative of (13)

$$\begin{aligned} \dot{\mathbf{V}}(\mathbf{e}, \tilde{\mathbf{K}}_y, \tilde{\mathbf{K}}_r) &= \dot{\mathbf{e}}^T \mathbf{P} \mathbf{e} + \mathbf{e}^T \mathbf{P} \dot{\mathbf{e}} + 2\text{tr}(\tilde{\mathbf{K}}_y^T \Gamma_y^{-1} \dot{\tilde{\mathbf{K}}}_y |\Lambda|) \\ &\quad + 2\text{tr}(\tilde{\mathbf{K}}_r^T \Gamma_r^{-1} \dot{\tilde{\mathbf{K}}}_r |\Lambda|) \\ &= \mathbf{e}^T (\mathbf{P}\mathbf{A}_m + \mathbf{A}_m^T \mathbf{P}) \mathbf{e} + 2\mathbf{e}^T \mathbf{P} \mathbf{B} \Lambda \left(\tilde{\mathbf{K}}_y^T \mathbf{y} + \tilde{\mathbf{K}}_r^T \mathbf{r} - \varepsilon_f(\mathbf{y}) \right) \\ &\quad + 2\text{tr} \left(\tilde{\mathbf{K}}_y^T \Gamma_y^{-1} \dot{\tilde{\mathbf{K}}}_y |\Lambda| \right) + 2\text{tr} \left(\tilde{\mathbf{K}}_r^T \Gamma_r^{-1} \dot{\tilde{\mathbf{K}}}_r |\Lambda| \right) \\ &= -\mathbf{e}^T \mathbf{Q} \mathbf{e} - 2\mathbf{e}^T \mathbf{P} \mathbf{B} \Lambda \varepsilon_f(\mathbf{y}) + 2\mathbf{e}^T \mathbf{P} \mathbf{B} \Lambda \tilde{\mathbf{K}}_y^T \mathbf{y} \\ &\quad + 2\text{tr} \left(\tilde{\mathbf{K}}_y^T \Gamma_y^{-1} \dot{\tilde{\mathbf{K}}}_y \right) + 2\mathbf{e}^T \mathbf{P} \mathbf{B} \Lambda \tilde{\mathbf{K}}_r^T \mathbf{r} + 2\text{tr} \left(\Delta \mathbf{K}_r^T \Gamma_r^{-1} \dot{\tilde{\mathbf{K}}}_r \right) \end{aligned}$$

Since $x^T y = \text{tr}(y x^T)$ from trace identity, we have

$$\begin{aligned} \dot{\mathbf{V}}(\cdot) &= -\mathbf{e}^T \mathbf{Q} \mathbf{e} - 2\mathbf{e}^T \mathbf{P} \mathbf{B} \Lambda \varepsilon_f \\ &\quad + 2\text{tr} \left(\tilde{\mathbf{K}}_y^T (\Gamma_y^{-1} \dot{\tilde{\mathbf{K}}}_y + \mathbf{y} \mathbf{e}^T \mathbf{P} \mathbf{B} \text{sgn}(\Lambda)) |\Lambda| \right) \\ &\quad + 2\text{tr} \left(\tilde{\mathbf{K}}_r^T (\Gamma_r^{-1} \dot{\tilde{\mathbf{K}}}_r + \mathbf{r} \mathbf{e}^T \mathbf{P} \mathbf{B} \text{sgn}(\Lambda)) |\Lambda| \right) \end{aligned} \quad (15)$$

where for a real-valued x , we have $x = \text{sgn}(x)|x|$. The first two terms in (15) will be negative definite for all $\mathbf{e} \neq 0$ since \mathbf{A}_m is Hurwitz and the other terms in (15) will be identically

null if we choose the adaptation laws

$$\dot{\tilde{\mathbf{K}}}_y = -\Gamma_y \mathbf{y} \mathbf{e}^T \mathbf{P} \mathbf{B} \text{sgn}(\Lambda), \quad \dot{\tilde{\mathbf{K}}}_r = -\Gamma_r \mathbf{r} \mathbf{e}^T \mathbf{P} \mathbf{B} \text{sgn}(\Lambda). \quad (16)$$

The time-derivative of the Lyapunov function can then be written as

$$\begin{aligned} \dot{\mathbf{V}}(\cdot) &= -\mathbf{e}^T \mathbf{Q} \mathbf{e} - 2\mathbf{e}^T \mathbf{P} \mathbf{B} \Lambda \varepsilon_f \\ &\leq -\lambda_{low} \|\mathbf{e}\|^2 + 2\|\mathbf{e}\| \|\mathbf{P}\mathbf{B}\| \lambda_{high}(\Lambda) \varepsilon_{max}, \end{aligned} \quad (17)$$

where $\lambda_{low}, \lambda_{high}$ represent the minimum and maximum characteristic roots of Q and Λ respectively. $\dot{\mathbf{V}}(\cdot)$ is thus negative definite outside the compact set

$$\chi = \left(\mathbf{e} : \|\mathbf{e}\| \leq \frac{2\|\mathbf{P}\mathbf{B}\| \lambda_{high}(\Lambda) \varepsilon_{max}}{\lambda_{low}(\mathbf{Q})} \right). \quad (18)$$

and we conclude that the error \mathbf{e} is *uniformly ultimately bounded*. As \mathbf{e} converges to a neighborhood of 0, \mathbf{y} converges to a neighborhood of \mathbf{y}_m . From the stable model reference system in (5), \mathbf{y} converges to a neighborhood of \mathbf{r} . Note that asymptotic convergence of \mathbf{e} to zero is not guaranteed but the parametric errors are guaranteed to stay bounded.

B. Network Design

We require accurate mapping of temporally lagged patterns in inputs to output states, a dynamic nonlinear model of valve encoder values to sensor measurements that accurately maps $f(\cdot)$ in (4). We choose a LSTM [17] due to its capacity for long-term context memorization and inherent multiplicative units that avoid oscillating weights or vanishing gradients when error signals are backpropagated in time [17], [21]. LSTMs truncate gradients in the network where it is harmless by enforcing constant error flows through their *constant error carousels*. As a result, LSTMs are robustly more powerful for adaptive sequence-to-sequence modeling or mapping data that temporally evolve in time. Their biological model makes them more suitable for adaptive robotics such as soft robots than previously used artificial NNs such as feedforward networks [22], radial basis-functions [20], [23] or vanilla RNNs [24].

The NN model takes a memory-based concatenated vector of current inputs and past outputs as in (7), propagates them through three hidden layers, with each layer made up of $\{9, 6, 6\}$ neurons each, applies 30% dropout and then maps the last layer to a fully connected layer that generates valve torques. The architecture of the neuro-controller is shown in Fig. 4. The last layer is designed to generate appropriate valve torques based on an internal model of the plant. A self-tuning adaptive control law (with a feedforward regulation and state feedback component) adapts to the internal parameters of the plant to ensure stability of the system and bounded tracking of given trajectory. The overall network has neuron connection weights and thresholds of approximately 1,400. This makes search for a suitable controller feasible.

The LSTM model estimates a model $f(\mathbf{y})$, that minimizes the mean-squared error between predicted output $\hat{\mathbf{y}}(k)$ and

actual output $\mathbf{y}(k)$ according to

$$f(\mathbf{y}(k)) = \arg \min_w \mathbf{V}_N(w, \Phi(\mathbf{y})) \quad (19)$$

where $\mathbf{V}_N(w, \Phi(\mathbf{y})) = \sum_{t=1}^K \sum_{i=1}^n \frac{1}{2} (\hat{\mathbf{y}}_i(t) - \mathbf{y}_i(t))^2$, and $\Phi(\mathbf{y})$ is a regression vector as defined in (7) on a bounded interval $[1, N]$. (19) is minimized using stochastic gradient descent so that at each iteration, we update the parameters (weights) of the network \mathbf{w}_i based on the *ordered derivatives* of $\mathbf{V}_N(w, \Phi(\mathbf{y}))$ (Werbos [25]) i.e.

$$\mathbf{w}_{k+1} \leftarrow \eta \mathbf{w}_k - \alpha \sum_{i=1}^n \nabla_w \mathbf{V}(\mathbf{y}_i, \hat{\mathbf{y}}_i(\theta_k)). \quad (20)$$

η (set to 1) hastens the optimization in a direction of low but steepest descent in training error, and α is a sufficiently small learning rate (set to 5×10^{-3}), and $\nabla_w \mathbf{V}(\theta, \Phi(\mathbf{y}))$ is the derivative of \mathbf{V} with respect to w averaged over the k -th batch (we used a batch size of 50). We initialized the weights of Fig. 4 from a one-dimensional normal distribution with zero-mean and unit variance.

VI. EXPERIMENT: SOFT ACTUATORS CONTROL

The headpose is determined based on our formulation in IV. The 3-DOF pose of the head is made up of the state tuple $\{z(k), \theta(k), \phi(k)\}$.

A. Adaptive Control Parameters

We sample from the parameters of the trained network and we set $\hat{f}(\cdot)$ in (6) to the fully connected layer of samples from the network. We publish the control law from the neural network and subscribe in a separate node. The gains $\hat{\mathbf{K}}_y$ and $\hat{\mathbf{K}}_r$ in (16), were found by solving the ODEs iteratively using a single step of the integral of the solutions to $\dot{\hat{\mathbf{K}}}_y(t)$, $\dot{\hat{\mathbf{K}}}_r(t)$. Our solution is an implementation of the Runge-Kutta Dormand-Prince 5 ODE-solver available in the Boost C++ Libraries². We found a step-size of 0.01 to be realistic. \mathbf{y}_m in (5) is computed based on the solution to the forced response of the linear system,

$$\mathbf{y}_m(t) = e^{\mathbf{A}_m t} \mathbf{y}_m(0) + \int_0^t e^{\mathbf{A}_m(t-\tau)} \mathbf{B}_m \mathbf{r}(\tau) d\tau.$$

We set $\mathbf{y}_m(0) = \mathbf{y}(0)$ at $t = 0$ and for a settling time requirement of $T_s = 5 \text{secs}$ at which the response remains within 2% of final value, we find that

$$\mathbf{A}_m = \begin{bmatrix} -\frac{1334}{1705} & 0 & 0 \\ 0 & -\frac{1334}{1705} & 0 \\ 0 & 0 & -\frac{1334}{1705} \end{bmatrix}. \quad (21)$$

For a nonnegative \mathbf{Q} and a positive definite \mathbf{P} , the pair $(\mathbf{Q}, \mathbf{A}_m)$ will be observable (LaSalle's theorem) so that the dynamical system is globally asymptotically stable. After searching, we picked a positive definite $\mathbf{Q} = \text{diag}(100, 100, 100)$ for the dissipation energy in (17) and set $\mathbf{A} = I_{3 \times 3}$ so that solving the general form of the lyapunov

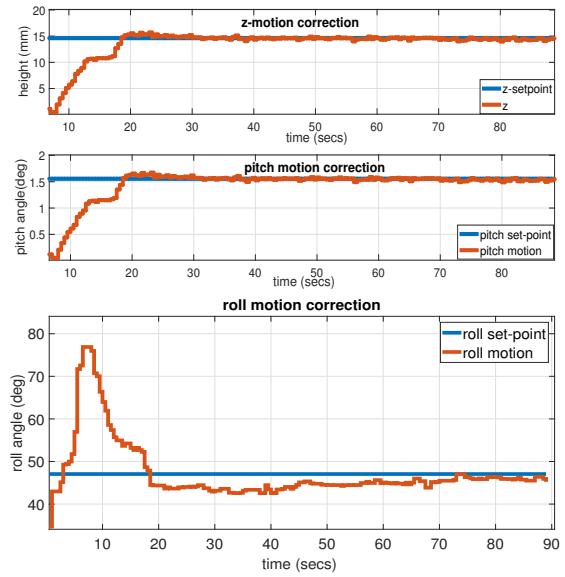


Fig. 5: Head motion correction along z, pitch and roll axes.

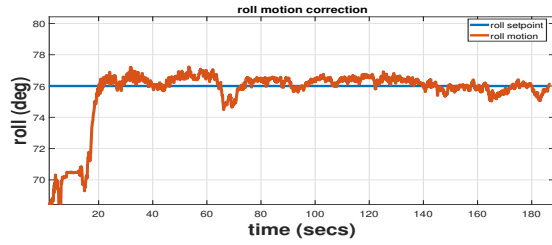


Fig. 6: Head motion correction along roll axis.

equation, we have

$$\mathbf{P} = \begin{bmatrix} -\frac{170500}{2668} & 0 & 0 \\ 0 & -\frac{170500}{2668} & 0 \\ 0 & 0 & -\frac{170500}{2668} \end{bmatrix} \quad (22)$$

The six solenoid valves operate in pairs so that two valves create a difference in air mass within each IAB at any given time. Therefore, we set

$$\mathbf{B} = \begin{bmatrix} 1 & 1 & 0 & 0 & 0 & 0 \\ 0 & 0 & 1 & 1 & 0 & 0 \\ 0 & 0 & 0 & 0 & 1 & 1 \end{bmatrix} \quad (23)$$

The non-zero terms in (23) denote the maximum duty-cycle that can be applied to the Dakota valves based on the software configuration of the NI RIO PWM generator.

B. Results and Analysis

The three DoFs of the head are coupled and there is a limited reachable space with the IABs. It is therefore paramount that desired trajectories be ascertained as physically realizable before rolling out control trials. We therefore placed the head to physically realizable positions in open-loop control settings before testing the close-loop control system on such feasible goal poses.

Fig. 5 show the performance of the controller when commanded to move the head from $[z, \theta, \phi]^T = [2.5 \text{mm}, .25^\circ, 35^\circ]^T$ to $[14 \text{mm}, 1.6^\circ, 45^\circ]^T$. We observe

²<https://goo.gl/l7JyYe>

strong steady-state convergence along 2-DoFs, namely z and pitch axes with a 20 second rise time. The roll motion is however characterized by offshoots that may be caused by the coupled DOF. We perform a second experiment, seen in Fig. 6, where we evaluate the performance of the controller on the roll angle of the head. We observe that the controller behaves well controlling the roll motion in isolation. The overshoot of Fig. 5 are likely due to coupled dynamics not accounted for in our formulation.

While our results are promising, showing the feasibility of the control law along the physically realizable axes of motions, the coupled degrees of freedom need further investigation to achieve independent and precise axial motion control whilst preserving global head goal requirements.

VII. DISCUSSION AND FUTURE WORK

We have presented a soft robot motion compensation system that uses a robust adaptive neurocontroller to correct patient positioning deviation in F&M RT along 3 degrees of freedom. Unlike related works that perform an inspection-based correction mechanism or employ radiation attenuating devices such as stepper motors positioned underneath the patient's head on the table, our method offers the elimination of reduction in the efficacy of dosage plans through compliant nonlinear soft elastomeric polymers. It also eliminates the pain of wearing metallic rings that rigidly immobilize a patient during treatment setups and dosage administration. The prospect of autonomously adapting to changing model parameters in our controller by learning compact and portable state representations of complex environments has widespread implications for autonomous robots.

Further research in this direction will focus on decoupling the control laws for the coupled states of the system whilst preserving global pose objectives. We are investigating control of custom-made multi-chambered air-bladders. Extensible to high-space DoF control, we will evaluate multiple soft-robot systems on a full-fledged human phantom and volunteer human trials.

REFERENCES

- [1] O. A. Zeidan, K. M. Langen, S. L. Meeks, R. R. Manon, T. H. Wagner, T. R. Willoughby, D. W. Jenkins, and P. A. Kupelian, "Evaluation of image-guidance protocols in the treatment of head and neck cancers," *International Journal of Radiation Oncology* Biology* Physics*, vol. 67, no. 3, pp. 670–677, 2007.
- [2] F. Sterzing, R. Engenhart-Cabillic, M. Flentje, and J. Debus, "Image-Guided Radiotherapy: A New Dimension in Radiation Oncology," *Deutsches Aerzteblatt International*, vol. 108, no. 16, p. 274, 2011.
- [3] J. Rossiter and H. Hauser, "Soft Robotics - The Next Industrial Revolution? [Industrial Activities]," *IEEE Robotics Automation Magazine*, vol. 23, no. 3, pp. 17–20, Sept 2016.
- [4] O. Ogunmolu, X. Gu, S. Jiang, and N. Gans, "A Real-Time Soft Robotic Patient Positioning System for Maskless Head-and-Neck Cancer Radiotherapy: An Initial Investigation," in *IEEE International Conference on Automation Science and Engineering*, Gothenburg, Sweden, Aug 2015.
- [5] O. Ogunmolu, X. Gu, S. Jiang, and N. Gans, "Vision-based Control of a Soft Robot for Maskless Head and Neck Cancer Radiotherapy," in *IEEE International Conference on Automation Science and Engineering*, Fort Worth, Texas, Aug 2016.
- [6] L. I. Cerviño, N. Detorie, M. Taylor, J. D. Lawson, T. Harry, K. T. Murphy, A. J. Mundt, S. B. Jiang, and T. A. Pawlicki, "Initial Clinical Experience with a Frameless and Maskless Stereotactic Radiosurgery Treatment," *Practical Radiation Oncology*, vol. 2, no. 1, pp. 54–62, 2012.
- [7] L. I. Cerviño, T. Pawlicki, J. D. Lawson, and S. B. Jiang, "Frame-less and mask-less cranial stereotactic radiosurgery: a feasibility study," *Physics in medicine and biology*, vol. 55, no. 7, p. 1863, 2010.
- [8] G. Li, A. Ballangrud, M. Chan, R. Ma, K. Beal, Y. Yamada, T. Chan, J. Lee, P. Parhar, J. Mechakos, et al., "Clinical Experience with two Frameless Stereotactic Radiosurgery (fsrs) Systems using Optical Surface Imaging for Motion Monitoring," *Journal of Applied Clinical Medical Physics/American College of Medical Physics*, vol. 16, no. 4, p. 5416, 2015.
- [9] X. Liu, A. H. Belcher, Z. Grelewicz, and R. D. Wiersma, "Robotic Stage for Head Motion Correction in Stereotactic Radiosurgery," in *American Control Conference (ACC), 2015*. IEEE, 2015, pp. 5776–5781.
- [10] E. Gmbh. Flexview. Accessed on January 21, 2016. [Online]. Available: <http://www.ensenso.com/products/flexview/>
- [11] R. B. Rusu, "Semantic 3D object Maps for Everyday Manipulation in Human Living Environments," *PhD thesis*, 2009.
- [12] A. Torr, Philip HS and Zisserman, "MLESAC: A New Robust Estimator with Application to Estimating Image Geometry," *Computer Vision and Image Understanding*, vol. 78, no. 1, pp. 138–156, 2000.
- [13] R. B. Rusu, Z. C. Marton, N. Blodow, M. E. Dolha, and M. Beetz, "Functional Object Mapping of Kitchen Environments," *2008 IEEE/RSJ International Conference on Intelligent Robots and Systems, IROS*, pp. 3525–3532, 2008.
- [14] R. B. Rusu and S. Cousins, "3D is here: Point Cloud Library (PCL)," in *IEEE International Conference on Robotics and Automation (ICRA)*, Shanghai, China, May 9–13 2011.
- [15] R. B. Rusu, A. Holzbach, M. Beetz, and G. Bradski, "Detecting and Segmenting Objects for Mobile Manipulation," in *Computer Vision Workshops (ICCV Workshops), 2009 IEEE 12th International Conference on*. IEEE, 2009, pp. 47–54.
- [16] N. D. Besl, Paul J.; McKay, "A Method for Registration of 3D Shapes." 1992.
- [17] S. Hochreiter and J. Schmidhuber, "Long Short-Term Memory," *Neural computation*, vol. 9, no. 8, pp. 1735–80, 1997.
- [18] P. Parks, "Liapunov Redesign of Model Reference Adaptive Control Systems," *IEEE Transactions on Automatic Control*, vol. 11, no. 3, pp. 362–367, 1966.
- [19] Y. D. Landau, *Adaptive Control: The Model Reference Approach*. Marcel Dekker, Inc, 1979.
- [20] E. Lavretsky and K. Wise, *Robust Adaptive Control with Aerospace Applications*. Springer, 2005.
- [21] B. Y. et al., "Learning Long-term Dependencies with gradient Descent is Difficult." *IEEE Transactions on Neural Networks*, 1994, doi: 10.1109/72.279181.
- [22] H. Dinh, S. Bhasin, R. Kamalapurkar, and W. E. Dixon, "Dynamic Neural Network-based Output Feedback Tracking Control for Uncertain Nonlinear Systems," *Journal of Dynamic Systems, Measurement, and Control*, 2017.
- [23] H. Patino and D. Liu, "Neural network-based model reference adaptive control system," *IEEE Transactions on Systems, Man, and Cybernetics, Part B (Cybernetics)*, vol. 30, no. 1, pp. 198–204, 2000.
- [24] J. S. Wang and Y. P. Chen, "A Fully Automated Recurrent Neural Network for Unknown Dynamic System Identification and Control," *IEEE Transactions on Circuits and Systems*, vol. 53, 2006.
- [25] P. J. Werbos, "Backpropagation Through Time: What It Does and How to Do It," *Proceedings of the IEEE*, vol. 78, no. 10, pp. 1550–1560, 1990.

Vision-based Control of a Soft Robot for Maskless Head and Neck Cancer Radiotherapy

Olalekan P. Ogunmolu¹, Xuejun Gu², Steve Jiang², and Nicholas R. Gans¹

Abstract—This work presents an on-going investigation of the control of a pneumatic soft-robot actuator addressing accurate patient positioning systems in maskless head and neck cancer radiotherapy. We employ two RGB-D sensors in a sensor fusion scheme to better estimate a patient’s head pitch motion. A system identification prediction error model is used to obtain a linear time invariant state space model. We then use the model to design a linear quadratic Gaussian feedback controller to manipulate the patient head position based on sensed head pitch motion. Experiments demonstrate the success of our approach.

I. INTRODUCTION

This paper presents a continuation of our investigation of an image-guided soft robot patient positioning system for use in head and neck (H&N) cancer radiotherapy (RT). In 2014, over 1.6 million patients developed pharynx and oral cavity cancers in the United States, which led to over 580,000 deaths [1]. Typical H&N cancer treatment involves intensity-modulated radiotherapy (IMRT), which delivers high potent dose to tumors while simultaneously minimizing dose to adjacent critical organs such as spinal cord, parotids glands, and optical nerves. Typically, a patient lies on a 6-DOF movable treatment couch, and laser or image-guidance systems are used to ensure the patient is in the proper position.

IMRT requires accurate patient positioning. An examination of patient displacement and beam angle misalignment during IMRT showed errors as small as 3-mm caused 38% decrease in minimum target dose or 41% increase in the maximum spinal cord dose [2]. Image-guided radiotherapy (IGRT) has improved IMRT accuracy while reducing set-up times [3], [4], [5]. However, current IGRT practices focus on using images acquired before treatment to confirm beam placement [6]. The discomfort caused by head masks in prolonged IMRT treatment can increase patients voluntary and involuntary motion. Studies show that translational errors caused by patient motion can be larger than 6mm, and rotational errors can be as high as 2° [7]. Current motion-tracking systems, such as Cyberknife and Novalis are not compatible with conventional linear particle accelerators used at the majority of cancer centers. Moreover, these two systems are limited to assuming the patient’s body is rigid during motion tracking and compensation. Recently, a robotic real-time surface image-guided positioning system was studied for feasibility in frameless and maskless cranial stereotactic radiosurgery [8]. While it achieved similar accuracy as the existing clinical methods, the system may not be suitable to IMRT due to the presence of mechanical and electrical parts in the path of the radiation beam.

Soft robot systems are deformable polymer enclosures with fluid-filled chambers that enable manipulation and locomotion tasks by a proportional control of the amount of fluid in the chamber [9], [10]. Their customizable, deformable nature and compliance make them suitable to biomedical applications as opposed to rigid and stiff mechanical robot components. They can also be made radiotransparent, which is necessary in IMRT.

The long term goal of our work is to address the non-rigid motion compensation during H&N RT. As we continue our initial investigation, we control one degree of freedom, raising or lowering of a generic patient’s head, lying in a supine position, to a desired height above a table. The current system consists of a single inflatable air bladder (IAB), a mannequin head and a neck/torso motion simulator, two different Kinect RGB-D cameras to measure patient position, two current-controlled pneumatic valve actuators, and a National Instruments myRIO microcontroller. In this work, we extended and improve our previous work [11]. This paper contributes better vision tracking and localization methods via filtering and fusion of the two RGB-D estimates. We improve on the system identification of the soft-robot system and now incorporate an optimal control network. The result is a much improved motion control.

Section II of this paper briefly presents the design of the soft robot system. Section III discusses the computer vision algorithms to detect the patient’s face and fusion of measurements from the RB-D images. Section IV presents results of system identification for the soft-robot system. Section V presents design of the linear quadratic Gaussian (LQG) controller, and Section VI presents several experiments to demonstrate the system.

II. SOFT ROBOT DESIGN OVERVIEW

The soft robot actuation mechanism combines an IAB (19” x 12”) made of lightweight, durable and deformable polyester and PVC, two current-controlled proportional solenoid valves, and a pair of silicone rubber tubes (attached to a T-port connector at the orifice of the IAB) in order to convey air in/out of the IAB. A 1HP air compressor supplied regulated air at 30 psi to the inlet actuating valve, while an interconnection of a 60W micro-diaphragm pump and a valve removed air from the outlet terminal of the IAB. The RGB-D sensors are mounted directly above the head for raw head position and velocity measurements, while local Kalman filters (KFs) provide two estimates of the head position and velocity. The sensor estimates are aggregated using a track-to-track KF-based sensor fusion algorithm. We apply the

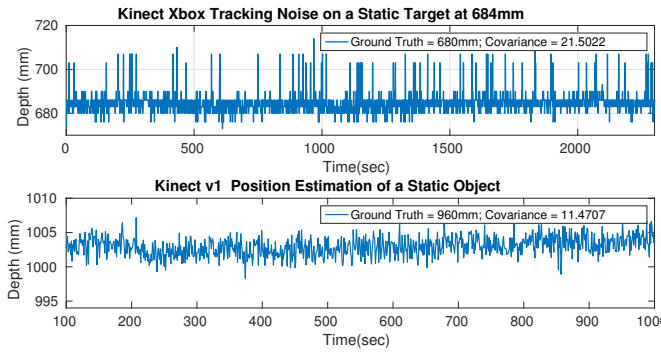


Fig. 1: Noise floor of Kinect Xbox Sensor vs. Kinect v2 Sensor

fusion result in a new robust control law for the pneumatic actuator valves, thereby regulating air pressure within the IAB and moving the patient's head as desired. The real-time controller was deployed on a National Instruments myRIO embedded system running LabVIEW 2015. The LabVIEW algorithms were processed within a Windows 7 virtualbox running on the Ubuntu host workstation.

We use a Kinect Xbox 360, and a Kinect for Windows v2 sensor to estimate head position and velocity. The two sensors use different electronic perception technologies to determine distance of an object from the camera origin. They therefore have different lateral and range resolutions as well as different noise characteristics. Image processing for both cameras is executed on a 22GB RAM mobile workstation with Intel Core i7-4800MQ processor running 64-bit Ubuntu Trusty on a Linux 4.04 kernel.

III. IMAGE-BASED PATIENT POSITION ESTIMATION

We perform recursive filter estimations of the RGB-D measurements and improve position estimates by using an additional sensor to better localize tracked features. We add the Kinect v2 sensor (henceforth called the v2 sensor), based on the time-of-flight (ToF) electronic perception principle. In ToF, light pulses illuminate a scene, and depth is calculated by determining the phase shift of the returned light signals. The active infra-red reduces the dependence on ambient lighting [12], and this sensor has a higher spatial depth resolution of 512×424 pixels at 30Hz interactive rate, compared to the Xbox's 320×240 pixels [13]. To minimize the noise due to the limited sensor resolution, the v2 has in-built noise improvement capabilities [14].

The v2 provides a higher depth-map accuracy and lower noise floor compared to Kinect for Xbox, as can be seen from Fig. 1, where the v2 exhibits a noise auto-covariance of 11.4707mm^2 compared with 22.7057mm^2 for the Xbox. Despite the improved performance of the v2, noise remains an issue, as is the case for every electronic perception system. To alleviate this, we employ a multisensor data fusion of both Kinect sensors' observations. We achieved this by local Kalman Filter estimates of each sensors observations, and we fuse the estimates via a variance-weighted multisensor Kalman filter fusion scheme described later in this section.

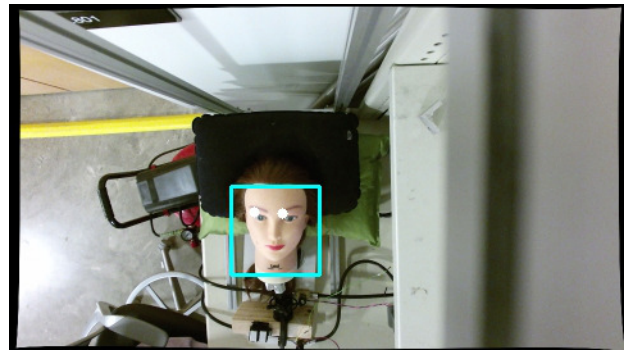


Fig. 2: Original colored image retrieved from the Kinect v2 Sensor.

A. Face Detection and eye-feature tracking

We approached face detection using Haar Cascade Classifiers (HCC) [15]. HCC's are based on integral image representation, which allow for features evaluation while maintaining high detection rates. The features resemble Haar basis functions. A classifier is formed by choosing a small number of crucial features with AdaBoost, and a weighted sum of individual classifiers is used to construct a strong object detection classifier in a cascade manner. This increases the detector's speed by concentrating on areas within an image with high probability of features of interest.

A drawback of HCC's is the memory consumed on computing devices when searching through image pixels for specific regions of interest. Searching through a 640×480 pixels gray-scale image for specific features caused a 90% reduction in the frame rates of either sensor, when the algorithm is run on a CPU. To overcome this, both sensor's images were spatially down-sampled via linear interpolation before HCCs were applied. Face detection was performed on a single NVIDIA Quadro K1100M GPU. We retrieve each detected face from the GPU, and then detect eyes within detected faces using the same procedure.

To achieve robust detection, the minimum number of neighbors in each candidate rectangle feature was determined based on our experience. The search area within an image was chosen to be within the range of (5×5) pixels and (20×20) pixels. This gave us more than 90% face detection rate for both sensors. A similar approach was used for the eye classifier. The final implementation achieved a frame rate of 15Hz for each sensor running independently on the Linux host computer. Further improvement in frame rates is an avenue for future work.

B. Local Kalman Filters

From Fig. 1, we see that both RGB-D sensors suffer from notable associated noise, which is not suitable for our control requirement. To refine the observation, local Kalman Filter (KF) estimates for each sensor were computed to determine state estimates $\hat{\mathbf{x}}(i)$ that minimizes the mean-squared error to the true state $\mathbf{x}(i)$, given a measurement

sequence $z(1), \dots, z(j)$, that is

$$\hat{\mathbf{x}}(i|j) = \arg \min_{\hat{\mathbf{x}}(i|j) \in \mathbb{R}^n} \mathbb{E}\{(\mathbf{x}(i) - \hat{\mathbf{x}})(\mathbf{x}(i) - \hat{\mathbf{x}})^T | z(1), \dots, z(j)\}$$

$$\triangleq \mathbb{E}\{\mathbf{x}(i)|z(1), \dots, z(j)\} \triangleq \mathbb{E}\{\mathbf{x}(i)|Z^j\} \quad (1)$$

where the obtained estimate is the expected value of the state at time i given observations up to time j . The covariance of the estimation error is given by

$$\mathbf{P}(i|j) \triangleq \mathbb{E}\{(\mathbf{x}(i) - \hat{\mathbf{x}}(i|j))(\mathbf{x}(i) - \hat{\mathbf{x}}(i|j))^T | Z^j\}. \quad (2)$$

Assuming the model of the state is common to both sensors, and denoting the distance from the v2 to the head as $d(k)$, we define $\mathbf{x}(k) = [d(k), \dot{d}(k)]^T \in \mathbb{R}^2$ as the state vector of interest, and let ΔT be the time between steps $k-1$ and k . The model state update equations are given by

$$\mathbf{x}_k = \mathbf{F}_k \mathbf{x}_{k-1} + \mathbf{B}_k \mathbf{u}_k + \mathbf{G}_k \mathbf{w}_k \quad (3)$$

where $\mathbf{F}(k) \in \mathbb{R}^{2 \times 2}$ is the state transition matrix given by

$$\mathbf{F} = \begin{bmatrix} 1 & \Delta T \\ 0 & 1 \end{bmatrix} \quad (4)$$

$\mathbf{u}(k) \in \mathbb{R}^2$ is the control input, $\mathbf{B}(k)$ is the control input matrix that maps inputs to system states, $\mathbf{G}(k) \in \mathbb{R}^{2 \times 2}$ process noise matrix, and $\mathbf{w}(k) \in \mathbb{R}^2$ is a random variable that models the state uncertainty. In the absence of inputs $\mathbf{B}_k \mathbf{u}_k = 0$, and the model becomes

$$\mathbf{x}_k = \mathbf{F}_k \mathbf{x}_{k-1} + \mathbf{G}_k \mathbf{w}_k \quad (5)$$

where \mathbf{w}_k is the effect of an unknown input and \mathbf{G}_k applies that effect to the state vector, \mathbf{x}_k . The process noise is assumed unknown and is modeled as uncontrolled forces causing an acceleration a_k in the head position (a_k is thus a scalar random variable with normal distribution, zero mean and standard deviation σ_a). We model this into (3) by setting \mathbf{G}_k to identity and set $\mathbf{w}(k) \sim \mathcal{N}(0, \mathbf{Q}(k))$ where the covariance matrix $\mathbf{Q}(k)$ is set to a random walk sequence defined by $\mathbf{W}_k = \left[\frac{\Delta T^2}{2}, \Delta T \right]^T$. Therefore, we find that

$$\mathbf{Q} = \mathbf{W} \mathbf{W}^T \sigma_a^2 = \begin{bmatrix} \frac{\Delta T^4}{4} & \frac{\Delta T^3}{2} \\ \frac{\Delta T^3}{2} & \Delta T^2 \end{bmatrix} \sigma_a^2. \quad (6)$$

Denoting the head displacement at time k as measured by the Xbox and v2 as $z_1(k)$ and $z_2(k)$ respectively, the sensors' measurements were mapped to the v2 reference frame and modeled as

$$z_s = \mathbf{H}_s(k) \mathbf{x}(k) + v_s(k) \quad s = 1, 2 \quad (7)$$

where $\mathbf{H}_s(k) = [1 \ 0]^T$ maps the system's state space into the observed space, and $v_s(k) \in \mathbb{R}$ is a random variable that models the sensor error. We define $v_s(k)$ as a normally distributed random variable with zero mean and variance σ_{rs}^2 . We assume the random sequences $v_1(k), v_2(k)$, $\mathbf{w}(k)$ are independent and uncorrelated in time.

At each time step, k , each local KF's priori and posteriori estimates are computed through the typical prediction and update phases

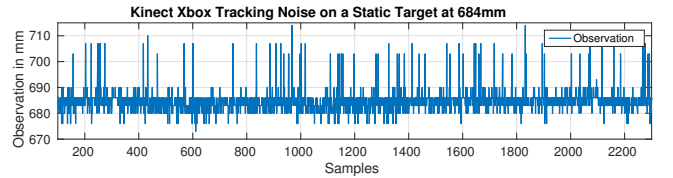


Fig. 3: KF results for the Xbox observation

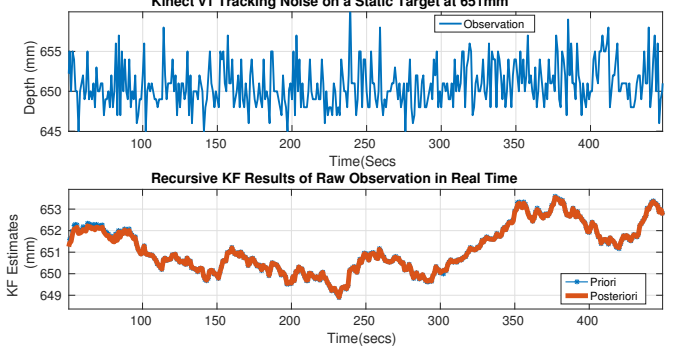


Fig. 4: KF results of Kinect v2's observation

Prediction Phase:

$$\hat{\mathbf{x}}(k|k-1) = \mathbf{F}(k) \hat{\mathbf{x}}(k-1|k-1) + \mathbf{B}(k) \mathbf{u}(k)$$

$$\mathbf{P}(k|k-1) = \mathbf{F}(k) \mathbf{P}(k-1|k-1) (\mathbf{F}(k))^T + \mathbf{Q}(k) \quad (8)$$

where $\hat{\mathbf{x}}(k|k-1)$ and $\mathbf{P}(k|k-1)$ are the state prediction vector and the prediction covariance matrix respectively.

Update Phase:

$$\mathbf{K}(k) = \mathbf{P}(k|k-1) \mathbf{H}(k)^T [\mathbf{H}(k) \mathbf{P}(k|k-1) \mathbf{H}(k)^T + \mathbf{R}(k)]^{-1}$$

$$\hat{\mathbf{x}}(k|k) = \hat{\mathbf{x}}(k|k-1) + \mathbf{K}(k) (\mathbf{z}(k) - \mathbf{H}(k) \hat{\mathbf{x}}(k|k-1))$$

$$\mathbf{P}(k|k) = (\mathbf{I} - \mathbf{K}(k) \mathbf{H}(k)) \mathbf{P}(k|k-1) \quad (9)$$

where \mathbf{K}_k , $\hat{\mathbf{x}}_{k|k}$, and $\mathbf{P}_{k|k}$ are respectively the KF gain, posteriori state estimate and its state covariance matrix. In implementing the KF of (8) and (9), the variance of the process noise/signal noise of each local KF was informed by our knowledge of the physics of both sensors (electronic perception methods, range resolutions and examining each sensor's depth map to understand the data available to the filter), engineering judgment, and kinematics of the process model. We found these values sufficiently modeled the underlying process dynamics

$$\sigma_a = 2000 \text{ mm}^2; \quad \sigma_{r1}^2 = 70 \text{ mm}^2 \text{ for the Xbox, and}$$

$$\sigma_{r2}^2 = 60 \text{ mm}^2 \quad \text{for the Kinect v2 sensor.}$$

Figs. 3 and 4 show the local filter estimate results of the observation from both the Kinect Xbox and v2 sensors post-filtering. The noise floor becomes noticeably reduced by each sensor after the KF filtering. The steady-state performance of both sensors include a reduction in the variance of the

observation sequence by 80.81%, while the Kinect v2 shows an improvement in noise rejection by almost 60% .

C. Data Fusion

Each local KF estimate was combined at a central fusion site to obtain a track-to-track fused global estimate. To communicate each estimate and associated covariance matrix, we create Unix FIFO special files (*i.e. named pipes*) on the kernel file system, write the estimates and covariance matrices to the pipes at each local site and retrieve the values at the central site.

Named pipes are low-level file I/O systems that can be shared by processes with different ancestry. During data exchange through a FIFO, the kernel forwards all data internally without having to write it to the file system. Since they exist within the kernel and the file system is just an entry serving as a reference point for the processes to access the pipe with a file system name, there is practically no delay in data communication.

Local tracks are generated at each sensor site according to (8), resulting in two local state predictions from the Kalman filters (3). At the central fusion site, we assume a state model common to both sensors given by (9) and adopt a variance-weighted average of each local track in the global track fusion algorithm [16]

$$\hat{\mathbf{x}}_F(k|k) = \mathbf{P}_F(k|k) \sum_{i=1}^N [\mathbf{P}_s^{-1}(k|k) \hat{\mathbf{x}}_s(k|k)]$$

$$\text{where } \mathbf{P}_F(k|k) = \left[\sum_{i=1}^N \mathbf{P}_s^{-1}(k|k) \right]^{-1}. \quad (10)$$

Fig. 5 shows the output of the fusion scheme compared against the single Kalman filters during a head-raising motion. The fusion of the local tracks produces better estimates, with improved signal to noise ratio. The fused estimate assigns more weight to the less noisy signal from Kinect v2. Through the implementation of the local tracks and a global track KF estimator, we improved the accuracy of the effective signal to be used in our control algorithm to no more than a standard deviation of 0.75mm from the true position of an object. The noise spikes in the fused tracks when the process state estimates are yet to converge as noticeable in Fig. 5 can be attributed to the noisy initialization of pixels in the sensors before they attain their steady state values. On average, it takes approximately 30 seconds for the pixel values in the Kinect sensor to reach their final steady state values [17]. This can be avoided by running the fusion algorithm for at least 2 minutes before the fused signal is used for any control purposes. The code for the multisensor fusion experiment is available on the git repos [18] and [19].

IV. SOFT ROBOT SYSTEM IDENTIFICATION

We approach the modeling procedure with an identification prediction error (PEM) approach, where we estimate a mathematical model, $G(t)$, based on the minimization of the

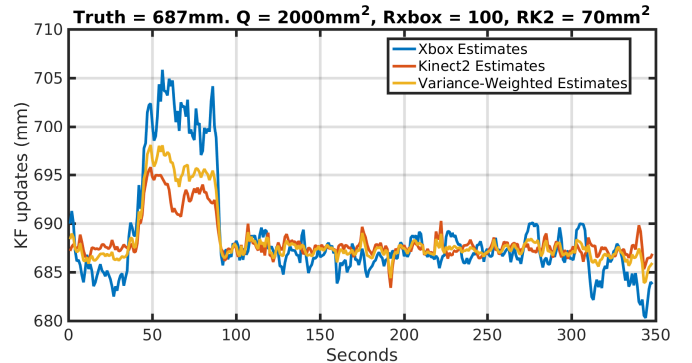


Fig. 5: Kalman filter Track-to-Track fusion of Kinect Xbox and v2's local tracks

sum of squared errors between estimates of the head height, $\hat{y}(t)$, and true head height, $y(t)$, from the fusion *i.e.*

$$G(t) = \arg \min_{\theta} V_N(\theta, Z^N)$$

$$\text{where } V_N(\theta, Z^N) = \sum_{k=1}^K \sum_{i=1}^n \frac{1}{2} (\hat{y}_i(k) - y_i(k))^2. \quad (11)$$

$Z^N = \{u(1) \cdots u(N) \ y(1) \cdots y(N)\}$ is the vector of past input and output (fused estimates) measurements over a bounded interval $[1, N]$ and θ is the greedy vector of parameters that approximate the model we seek to build. (11) is a special case of the least squares criterion.

A. Model Structure

Following Ljung's formulation in [20, §4.5], we pose the identification problem as determining the “best model” from a set of candidate model sets via an iterative approach that parametrizes the noncountable model sets smoothly over an area with the assumption that the underlying system is linear time-invariant. Here, our model structure is a differentiable mapping from a connected, compact subset $\mathcal{D}_{\mathfrak{M}}$ of \mathcal{R}^d to a model set \mathfrak{M}^* , such that the gradients of the predictor functions are stable. This procedure is included in the MATLAB system identification toolbox, and since the method is well-documented in [21] we omit details.

External disturbances and stochastic variables are modeled as additive white noise sequence, $e(k)$, based on lagged inputs and outputs, and our objective is to estimate a stochastic state space model structure of the form

$$\begin{aligned} \mathbf{x}(k+1) &= \mathbf{A}\mathbf{x}(k) + \mathbf{B}\mathbf{u}(k) + \mathbf{w}(k) \\ \mathbf{y}(k) &= \mathbf{C}\mathbf{x}(k) + \mathbf{D}\mathbf{u}(k) + \mathbf{v}(k) \end{aligned} \quad (12)$$

where the noise terms $\mathbf{w}(k)$ and $\mathbf{v}(k)$ compensate for the effect of disturbances beyond frequencies of interest to system dynamics and make the model robust to model uncertainties. Since \mathbf{u} and \mathbf{y} alone are measurable in our setup, the states $\mathbf{x}(k)$ are estimated and (12) becomes a linear regression problem, where all the unknown matrix entries are linear

combinations of the measured inputs and output variables. This can be written as

$$Y(k) = \Theta\Phi(k) + E(k) \quad (13)$$

where

$$Y(k) = \begin{bmatrix} \mathbf{x}(k+1) \\ \mathbf{y}(k) \end{bmatrix}, \quad \Theta = \begin{bmatrix} \mathbf{A} & \mathbf{B} \\ \mathbf{C} & \mathbf{D} \end{bmatrix}$$

$$\Phi(k) = \begin{bmatrix} \mathbf{x}(k) \\ \mathbf{u}(k) \end{bmatrix} \text{ and } E(k) = \begin{bmatrix} \mathbb{E}(w(k)) \\ \mathbb{E}(v(k)) \end{bmatrix}.$$

We assume the noise term is white in order to assure an unbiased model. The parameter estimation problem is then to estimate the \mathbf{A} , \mathbf{B} , \mathbf{C} , and \mathbf{D} matrices by the linear least squares regression of (13) assuming no physical insight into the system (i.e. a black box model). $\mathbb{E}(\mathbf{w}(k))$ and $\mathbb{E}(\mathbf{v}(k))$ are estimated as a sampled sum of squared errors of the residuals.

B. Parameter Estimation

The input, $u(k)$, and output signals, $y(k)$, can be characterized by a linear difference equation of the form

$$\begin{aligned} y(k) &= -a_1 y(k-1) - \cdots - a_{n_a} y(k-n_a) \\ &- b_1 u(k-1) - \cdots - b_{n_b} u(k-n_b) - e(k) \\ &- c_1 e(k-1) - c_{n_c} e(k-n_c) \end{aligned} \quad (14)$$

where $e(k)$ describes the equation error as a moving average of white noise, and we assume $e(k)$ has a bias-variance term λ . We can rearrange (14) using the vectors

$$\begin{aligned} \psi(k, \theta) &= [-y(k-1) \cdots -y(k-n_a) \ u(k-1) \cdots \\ &\quad u(k-n_b), \ e(k-1, \theta), \dots, e(k-n_c, \theta)]^T \end{aligned} \quad (15)$$

$$\theta = [-a_1, \dots, -a_{n_a}, -b_1, \dots, -b_{n_b}, -c_1, \dots, -c_{n_c}]. \quad (16)$$

The adjustable parameters of (15) are elements of θ . In our prediction model, it is convenient to write (14) as a one-step-ahead predictor of the form

$$\hat{y}(k) = G(q, \theta)u(k) + H(q, \theta)\hat{e}(k) \quad (17)$$

$$\text{with } G(q, \theta) = \frac{B(q)}{A(q)}, \quad H(q, \theta) = \frac{C(q)}{A(q)}$$

which is a complete autoregressive moving average with exogenous input (ARMAX) model. $G(q, \theta)$ represents the transfer function from input to output predictions, and $H(q, \theta)$ denotes the transfer function of prediction errors to the output model, $\hat{y}(k)$; q is the z-transform, z^{-1} , while $A(q)$, $B(q)$, and $C(q)$ are polynomials defined as

$$\begin{aligned} A(q) &= 1 + a_1 q^{-1} + \cdots + a_{n_a} q^{-n_a}, \\ B(q) &= b_1 q^{-1} + \cdots + b_{n_b} q^{-n_b}, \\ C(q) &= 1 + c_1 q^{-1} + \cdots + c_{n_c} q^{-n_c} \end{aligned} \quad (18)$$

[22]. The predictor turns out to be a linear filter of the form

$$\hat{y}(k|\theta) = W_y(q, \theta)y(k) + W_u(q, \theta)u(k) \quad (19)$$

$$\text{and } y(k) = G(q, \theta)u(k) + H(q, \theta)[y(k) - \hat{y}(k)] \quad (20)$$

where $H(q, \theta)$ is the noise model and $\hat{y}(k)$ above can be regarded as the one-step ahead predictor. After rearranging (19), we find that

$$W_y = 1 - H^{-1}(q, \theta) \text{ and } W_u(q, \theta) = G(q, \theta)H^{-1}(q, \theta)$$

such that the residual errors from (19) become

$$e(k) = [y(k) - G(q, \theta)u(k)]H^{-1}(q, \theta). \quad (21)$$

We can consider (21) as passing the prediction errors through a linear filter that allows extra freedom in dealing with non-momentary properties of the prediction errors. Since the model is that of a linear system, (21) satisfies our objective by approximating the prefilter with the choice of the noise model in (13).

The estimation problem is to predict the estimates, $\hat{y}(k|\theta)$ so that the errors, $\varepsilon(t, \theta) = \|y(t) - \hat{y}(t|\theta)\|_p$ are minimized by the choice of an appropriate p-norm criterion function, such as the mean squared error proposed in (11).

1) Input Signal Design: The input signal choice for a system identification experiment will determine a system's operating point and model accuracy. Therefore, the input should be rich enough to excite a system and force it to show properties needed for the model's purpose. For the model to be informative across all the desired frequency range, a periodic, persistently exciting uniform Gaussian White noise (UGWN) signal with clipped amplitudes corresponding to the bandwidth of the valves was designed offline, and its frequency spectrum analyzed to ensure it had as small a crest factor as possible (since the asymptotic properties of the model will be mostly influenced by the spectrum rather than the waveform's time-series shape). Gaussian White Noise signals (GWN) and Pseudo-Random Binary Signals (PRBS) are well-known to achieve virtually any signal spectrum without very narrow pass bands. Therefore, pseudo-random uniform white noise sequences were generated using the very-long cycle random number generator algorithm. Given that the probability density function, $f(x)$, of the uniformly distributed uniform white noise is

$$\begin{aligned} f(x) &= \frac{1}{2}A && \text{if } x < |A| \text{ and} \\ u(x) &= 0 && \text{if } x > |A| \end{aligned} \quad (22)$$

where A is the amplitude. The expected mean, μ , and the expected standard deviation, σ of the sequence are [23]

$$\mu = \mathbb{E}(x) = 0, \quad \sigma = [\mathbb{E}\{(x - \mu)\}]^{\frac{1}{2}} = \frac{A}{\sqrt{3}}. \quad (23)$$

The spectrum of the resulting signal in Fig. 6 gives good signal power, which nicely relates to the bandwidth of the pneumatic valves and achieves virtually all signal spectrum with little narrow pass bands.

We therefore use the signal of (22) to model the desired asymptotic estimates, $\hat{y}(t)$, of (17). We sampled $y(t)$, the fused measurement described in (III-C) well-above the system's Nyquist frequency and acquired enough samples to make Z^N asymptotically approach $\hat{\theta}_N$ as $N \rightarrow \infty$. The data collection procedure closely follows that described in

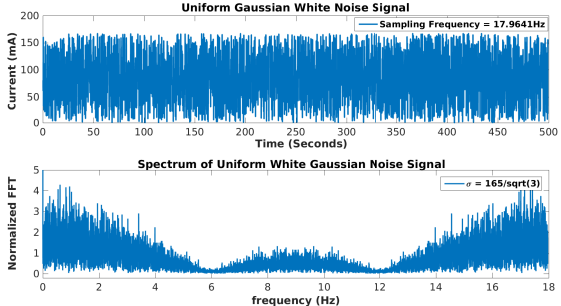


Fig. 6: Time/Frequency-Domain Properties of the Input Signal

our previous paper and we refer readers to [11, §IV.A] for a more detailed treatment.

The collected data was separated in a 60:40% ratio for training and testing purposes, respectively, to assure a training model that generalizes well.

2) *State Space Realization:* If we define

$$\hat{Y}_r(k) = [\hat{y}(k|k-1), \dots, \hat{y}(k+r-1)|k-1]^T$$

$$\hat{Y} = [\hat{Y}_r(1) \dots \hat{Y}(N)],$$

it follows that 1) as $N \rightarrow \infty$, there are n -th order minimal state space descriptions of the system if and only if the rank of the matrix of prediction vectors, \hat{Y} , is equal to n for all $r \geq n$; and 2) the state vector of any minimal realization in innovations can be chosen as linear combinations of \hat{Y}_r that form a row basis for \hat{Y} , i.e.,

$$x(t) = L\hat{Y}_r(k)$$

with L being an $n \times pr$ matrix (p is the dimension of $y(k)$) [20, §7.3]. The true prediction is given by (17) with innovations $e(j)$ written as a linear combination of past input-output data. The predictor can thus be expressed as a linear function of $u(i)$, $y(i)$, $i \leq k-1$. In practice, the predictor is approximated so that it depends on a finite amount past data such as s_1 past outputs and s_2 past inputs of the form

$$\hat{y}(k|k-1) = \alpha_1 y(k-1) + \dots + \alpha_{s_1} y(k-s_1) \quad (24)$$

$$+ \beta_1 u(k-1) + \dots + \beta_{s_2} u(k-s_2).$$

Piping the identification data through the MATLAB function ‘ssest’ and testing various model orders based on the ranking of singular values of the Hankel matrix of input-output measurements [20], we obtained the results listed in Table I on training and testing dataset. The MATLAB system identification script is provided on a github repo [24] and contains the dataset used for the experiment. The model set above exhibit a high-fit of estimate to fed data with generally good mean-square errors and final prediction errors for a control experiment. With increasing model order starting

TABLE I: Model estimates

Data Type	Expts	MO ¹	MSE ²	Fit (%)	FPE ³
Training	i	2	0.001437	97.64	0.001438
	ii	4	0.001454	97.62	0.00145584
	iii	6	0.001333	97.72	0.001336
	iv	8	0.001298	97.76	0.001298
Testing	i	2	0.000963	98.47	0.000964
	ii	4	0.0008574	98.56	0.008594
	iii	6	0.000846	98.57	0.000849
	iv	8	0.000843	98.57	0.000848

from 4, we see that the fits start reaching convergence, as the mean-square errors and final prediction errors become constant. In the frequency-domain, this is the equivalent to having pole-zero cancellations for higher-order models. We therefore conclude there is no useful properties a higher-order model could predict beyond an order of 8. The second-order model sufficiently approximates the system and is not significantly outperformed by the higher order models –which would contribute higher complexity to the control design. We therefore pick the 2nd order state space model (12) as

$$\mathbf{x}(k+Ts) = \mathbf{Ax}(k) + \mathbf{Bu}(k) + \mathbf{Ke}(k)$$

$$\mathbf{y}(k) = \mathbf{Cx}(k) + \mathbf{Du}(k) + \mathbf{e}(k) \quad (25)$$

where Ts is the sampling period, $\mathbf{e}(k)$ is the modeled zero-mean Gaussian white noise with non-zero variance,

$$\mathbf{A} = \begin{bmatrix} 0 & 1 \\ -0.9883 & 1.988 \end{bmatrix}, \quad \mathbf{B} = \begin{bmatrix} -3.03e-07 \\ -4.254e-07 \end{bmatrix}$$

$$\mathbf{C} = [1 \ 0], \quad D = 0, \text{ and } \mathbf{K} = [0.9253 \ 0.9604]^T. \quad (26)$$

The pair (A, B) is stabilizable and the pair (A, C) is detectable.

V. LQG CONTROL

We employ a LQG controller and estimator to minimize the following cost function subject to the state equation (26)

$$J = \sum_{k=0}^{\mathcal{K}} x^T(k) Q x(k) + R u(k)^T u(k) + 2x(k)^T N u(k) \quad (27)$$

where \mathcal{K} is the terminal sampling instant, Q is a symmetric, positive semi-definite matrix that weights the n -states of the A matrix, N specifies a matrix of appropriate dimensions that penalizes the cross-product between the input and state vectors, while R is a symmetric, positive definite weighting matrix on the control vector u . The quadratic cost function in (27) allows us to find an analytical solution (controller sequence) to the minimization of J over the prediction horizon, n_y

$$\Delta u = \arg \min_{\Delta u} J \quad (28)$$

where Δu is the future control sequence and the first element in the sequence is used in the control law at every time instant. We model additive white noise disturbances into

¹Model Order

²Mean Squared Error (mm^2).

³Akaike Final Prediction Error ([20, Secs 7.4 and 16.4]).

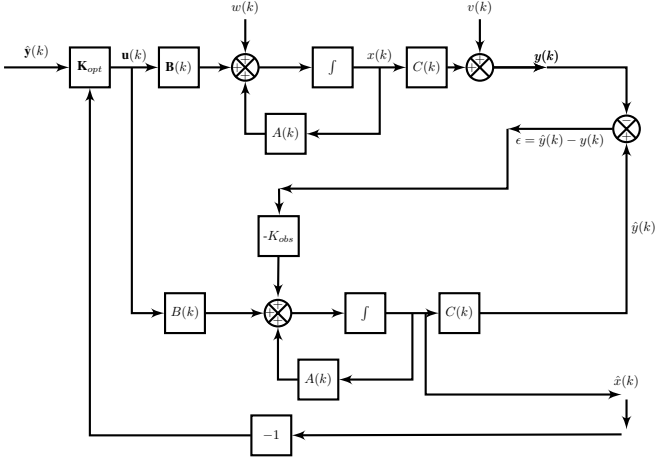


Fig. 7: Full Linear Quadratic Gaussian Plant Estimator

the discrete estimator's states; therefore the optimization problem becomes a stochastic optimization problem that must be solved.

The separation theorem ensures that we can construct a state estimator which asymptotically tracks the internal states from observed outputs, $y(k)$, using the algebraic Riccati equation given as

$$A^T P A - (A^T P B + N)(R + B^T P B)^{-1}(B^T P A + N) + Q. \quad (29)$$

where P is an unknown $n \times n$ symmetric matrix and A , B , Q , and R are known coefficient matrices as in (26) and (27). We find an optimal control law by solving the minimization of the LQ problem, (27) which we then feed into the states.

In practice, it is a good idea to start with an identity matrix, Q , a zero penalty matrix, N , and tune R till one obtains convergence by the state estimator. The following optimal values were used after a heuristic search

$$Q = \begin{bmatrix} 1.0566 & 0 \\ 0 & 1.0566 \end{bmatrix}, \quad R = [0.058006]. \quad (30)$$

We construct a full online estimator for the identified plant as in Fig. 7, whereby the noise processes are assumed to be independent, white, Gaussian, of zero mean and known covariances. The optimal controller gains, K_{opt} , are determined from the equation

$$K_{opt} = R^{-1}(B^T P + N^T) \quad (31)$$

[25] where P is the solution to the algebraic Riccati equation (29) and $\mathbb{E}[w(k)w'(\tau)] = R(k)\delta(k - \tau)$. Therefore, the online optimal estimate, $\hat{x}(k+1)$ of $x(k)$ is

$$\hat{x}(k+1) = A(k)\hat{x}(k) + K_{lqg}[C(k)\hat{x}(k) - y(k)] \quad (32)$$

where $\hat{x}(k_0) = \mathbb{E}[x(k_0)]$. The observer is equivalent to a discrete stochastic Kalman filter that estimates the optimal state $\hat{x}(k|k)$ as shown in Fig. 7. The estimator equations are similar to equations (8) and (9) and the online, unbiased estimate is

$$\begin{aligned} \hat{x}(k+1) &= A(k)\hat{x}(k) - K_{obs}[\hat{y}(k) - y(k)] + B(k)u(k) \\ \hat{y}(k) &= C(k)\hat{x}(k) \end{aligned} \quad (33)$$

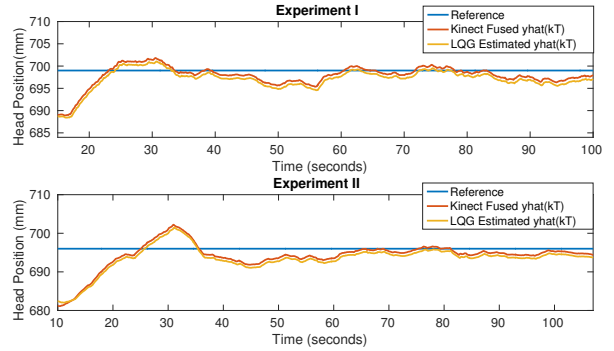


Fig. 8: LQG Controller on Manikin Head

\implies

$$\begin{aligned} \hat{x}(k+1) &= A(k)\hat{x}(k) - K_{obs}[C(k)\hat{x}(k) - y(k)] \\ &\quad + B(k)u(k). \end{aligned} \quad (34)$$

Through heuristics, we found the following variances of the online estimator to be useful:

$$Q_e = \begin{bmatrix} 0.4511 & 0 \\ 0 & 0.4511 \end{bmatrix}, \quad R_e = [0.01]$$

VI. EXPERIMENTAL RESULTS AND DISCUSSION

The control network was implemented on an NI-myRIO running LabVIEW 2015. We initialized the Kinect sensors to allow for all pixels within the depth cameras to reach steady state under ambient light. We performed multiple experiments to evaluate the developed state space model of IV-B and LQG controller of V.¹. The input variable is the current that excites the valve, which in turn actuates the bladder; the head moves in response to bladder actuation. The fused estimate of the Kinect sensors are used to estimate the real-time head pitch motion as described in III-C; this is in turn used in a feedback to the LQG controller.

Fig. 8 shows the results from a constant reference trajectory, which the head is meant to track. We notice a settling time of approximately 24 seconds before we reach steady state. The delay arises from our design requirements and is not a drawback in clinical trajectory tracking where we must ensure smooth head motion to desired target. It is also seen that the controller exhibits relatively smooth tracking within a 1.5 mm standard deviation over time after a relative overshoot of 5mm in bottom graph of Fig. 8. The overshoot can be explained by the estimator's search for a steady state region based on the time it takes for the pixel values of the sensors to reach steady state. The controller tracks the reference to within $\pm 2\text{mm}$.

However, we noticed an inconsistency at certain operating ranges in the current LTI model. The applied current based on fusion feedback occasionally reaches a steady state error, as can be seen from Fig. 9. We conjecture this is due to an unmodeled nonlinearity at the inlet valve that maps input currents to system states. To better approximate the

¹The LabVIEW identification and control codes are available on the git repo [26].

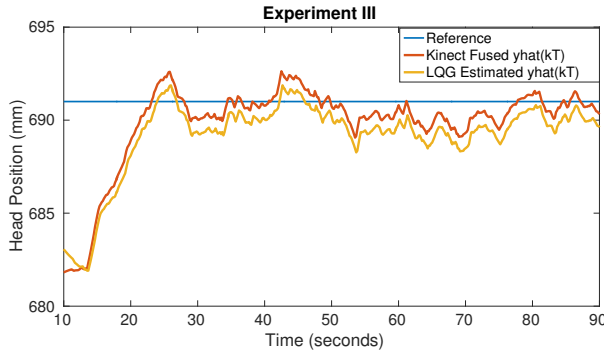


Fig. 9: LQG Controller on Manikin Head

nonlinearity from input to output, we will investigate using a Hammerstein block-structured model that better approximates the nonlinearity from inputs to states and states to output of the system.

The fusion algorithm proved useful to cancel jitter in the depth measurement of the sensor over our previous results, but it falls short of the 1mm accuracy in head and neck cancer RT. Having established proof of concept in this investigation, we will begin investigation of better head localization by using sophisticated motion capture systems or laser scanners, such as those actively employed in IGRT.

VII. SUMMARY

We have presented a continuation of our initial investigation into a pneumatically-driven soft robot system for head and neck radiotherapy. Measurements from two Kinect RGB-D cameras are fused to refine the accuracy of observations. System identification on the soft robot was combined with LQG controller design to provide an optimal controller. Experiments showed we could actuate the patient head within 2.5mm accuracy. Future work will investigate accurate multi-axis positioning using better 3D sensor, control of multiple IABs, and nonlinear modeling or model free-methods to overcome limitations of the LTI model.

REFERENCES

- [1] R. Siegel *et al.*, "Cancer statistics," *CA: A Cancer Journal for Clinicians*, vol. 64, no. 1, pp. 9–29, 2014.
- [2] L. Xing, "Dosimetric effects of patient displacement and collimator and gantry angle misalignment on intensity modulated radiation therapy," *Radiother Oncol*, vol. 56, no. 1, pp. 97–108, 2000.
- [3] T. Takakura *et al.*, *The geometric accuracy of frameless stereotactic radiosurgery using a 6D robotic couch system*. Phys Med Biol, 2010.
- [4] P. H. Ahn *et al.*, "Random positional variation among the skull, mandible, and cervical spine with treatment progression during head-and-neck radiotherapy," *Int J Radiat Oncol Biol Phys*, vol. 73, no. 2, pp. 626–33, 2009.
- [5] D. Robb *et al.*, "Assessing the efficiency and consistency of daily image-guided radiation therapy in a modern radiotherapy centre," *Journal of Medical Imaging and Radiation Sciences*, 2013.
- [6] D. Jaffray, "Image-guided radiotherapy: from current concept to future perspectives," *Nat Rev Clin Oncol*, vol. 9, no. 12, pp. 688–699, 2012.
- [7] H. Kang, D. M. Lovelock, E. D. Yorke, S. Kruminiski, N. Lee, and H. I. Amols, "Accurate positioning for head and neck cancer patients using 2d and 3d image guidance," *J Appl Clin Med Phys*, vol. 12, no. 1, p. 3270, 2011.
- [8] L. I. C. T. P. J. D. Lawson and S. B. Jiang, "Frame-less and mask-less cranial stereotactic radiosurgery: a feasibility study," *Phys. Med. Biol.*, vol. 55, pp. 1863–1873, 2010.

- [9] C. Laschi *et al.*, "Soft robot arm inspired by the octopus," *Advanced Robotics*, vol. 26, no. 7, pp. 709–727, 2012.
- [10] P. Maeder-York, T. Clites, E. Boggs, R. Neff, P. Polygerinos, ó. Holland, L. Stirling, K. Galloway, C. Wee, and C. Walsh, "Biologically inspired soft robot for thumb rehabilitation," *Journal of Medical Devices*, vol. 8, no. 2, p. 020933, 2014.
- [11] O. Ogunmolu, X. Gu, S. Jiang, and N. Gans, "A Real-Time Soft Robotic Patient Positioning System for Maskless Head-and-Neck Cancer Radiotherapy: An Initial Investigation," in *IEEE International Conference on Automation Science and Engineering*, Gothenburg, Sweden, Aug 2015.
- [12] (2015) Kinect Hardware. [Online]. Available: <https://dev.windows.com/en-us/kinect/hardware>
- [13] (2015) Constants. [Online]. Available: <https://msdn.microsoft.com/en-us/library/hh855368>
- [14] H. Gokturk, S.B. Yalcin and C. Bamji, "A Time-of-Flight Depth sensor - System Description, Issues and Solutions," in *2004 Conference on Computer Vision and Pattern Recognition Workshop*, 2004.
- [15] P. Viola and M. Jones, "Rapid Object Detection using a Boosted Cascade of Simple Features," pp. 511–518.
- [16] H. Durrant-Whyte. (2001, Jan) Introduction to Estimation and the Kalman Filter. Accessed Aug 05, 2015. [Online]. Available: http://www.dynsyslab.org/archive/RecEst2010/www.idsc.ethz.ch/Courses/Archives/Recursive_Estimation/recursive_filtering_2010/EstimationNotes.pdf
- [17] Andersen *et al.* (2012) Kinect Depth Sensor Evaluation for Computer Vision Applications. Accessed on Feb 23, 2016. [Online]. Available: http://eng.au.dk/fileadmin/DJF/ENG/PDF-filer/Tekniske_rapporter/Technical_Report_ECE-TR-6-samlet.pdf
- [18] O. Ogunmolu. (2015) Face Tracker with the Xbox Sensor. Accessed on Feb. 24, 2016. [Online]. Available: https://github.com/lakehanne/xbox_tracker
- [19] ———. (2015) IAI_Kinect2. Accessed on Feb. 24, 2016. [Online]. Available: https://github.com/lakehanne/iai_kinect2
- [20] L. Ljung, *System Identification Theory for the User*, 2nd ed. Upper Saddle River, NJ, USA.: Prentice Hall, 1999.
- [21] L. Ljung, *System Identification Toolbox™ User's Guide R2014b*, Natick, MA, 2014.
- [22] S. Billings, *Nonlinear System Identification: NARMAX Methods in the Time, Frequency, and Spatio-Temporal Domains*. John Wiley and Sons,Ltd, 2013, vol. 39, no. 3.
- [23] N. Instruments. (2011) Uniform white noise vi - labview 2011. Accessed on March 26, 2016. [Online]. Available: http://zone.ni.com/reference/en-XX/help/371361H-01/lvanls/uniform_white_noise/
- [24] O. Ogunmolu. (2015) Black Box Identification for Control. Accessed on Feb. 24, 2016. [Online]. Available: https://github.com/SeRViCE-Lab/Matlab-Files/blob/master/ident_data/Filtered%20GWN/carimaFWGN.m
- [25] B. Anderson and J. Moore, *Optimal Control: Linear Quadratic Methods*. Prentice Hall, Englewood Cliffs, New Jersey 07632, 1990.
- [26] O. Ogunmolu. (2015) RAL-Codes. Accessed on Feb 24, 2015. [Online]. Available: https://github.com/SeRViCE-Lab/RAL-Codes/blob/master/LQG%20Design/Soft_Robot_Model_ffwd.vi

Real-Time, Soft Robotic Patient Positioning System for Maskless Head-and-Neck Cancer Radiotherapy

Olalekan P. Ogunmolu¹, Xuejun Gu², Steve Jiang², and Nicholas R. Gans¹

Abstract—We present an initial examination of a novel approach toward accurately positioning a patient during head and neck intensity modulated radiotherapy (IMRT). Position-based visual-servoing of a radio-transparent soft robot is used to control the flexion/extension cranial motion of a manikin head. A Kinect RGB-D camera is used to measure head position and the error between the sensed and desired position is used to control a pneumatic system which regulates pressure within an inflatable air bladder (IAB). Results show that the system is capable of controlling head motion to within 2mm with respect to a reference trajectory. This establishes proof-of-concept that using multiple IABs and actuators can improve cancer treatment.

Index Terms - Life Sciences and Health Care; Mechatronics; Emerging Topics in Automation

I. INTRODUCTION

This paper presents a systematic initial examination of an image-guided soft robot patient positioning system for use in head and neck (H&N) cancer radiotherapy (RT). H&N cancers are among the most fatal of major cancers. In 2014, 1,665,540 new patients developed pharynx and oral cavity cancers which led to 585,720 deaths in the United States [1]. Treating these cancers often involve intensity modulated radiotherapy (IMRT) where a patient lies on a 6-DOF movable treatment couch and lasers or image-guiding systems are used to ensure the patient is in the proper position. A linear accelerator (LINAC) is used to accelerate electrons in a wave guide to enable collision of electrons with a heavy metal target. High-energy x-rays produced from the collisions are shaped by multileaf collimators as they exit the gantry of the machine to conform to the shape of the patient's tumor. The beam that emerges can be directed to a tumor from any angle by rotating the gantry and moving the couch.

IMRT requires accurate patient positioning while high potent dose radiation is delivered to tumor while sparing critical organs nearby. An examination of dosimetric effects on patient displacement and collimator and gantry angle misalignment during IMRT showed high sensitivity to small perturbations: a 3-mm error in anterior-posterior direction caused 38% decrease in minimum target dose

*This work was supported by the Radiation Oncology Department, UT Southwestern, Dallas, Texas, USA

¹Olalekan P. Ogunmolu and Nicholas R. Gans are with the Department of Electrical Engineering, University of Texas at Dallas, Richardson, TX 75080, USA {olalekan.ogunmolu, ngans}@utdallas.edu

²Xuejun Gu and Steve Jiang are with the Department of Radiation Oncology, University of Texas Southwestern Medical Center, Dallas TX 75390, USA {Xuejun.Gu, Steve.Jiang}@utsouthwestern.edu

or 41% increase in the maximum spinal cord dose [2]. Treatment discomfort and severe pain often results from long hours of minimally invasive surgery where the skull is fixed with pins for head immobilization during stereo-tactic radiosurgery (SRS). In addition, conventional linear accelerators (LINACs) used at most cancer centers are insufficient for the high geometric accuracy and precision required of SRS for isocenter localization [3].

Image-guided radiotherapy (IGRT) has made progress in improving accuracy while reducing set-up times [3], [4], [5]. The Robotic Tilt Module (RTM) interfaced with an image-guidance system [3], [6] enables high-precision positional correction by automatically aligning the patient when the image-guidance system detects positional errors. However, the power of IGRT hasn't been fully explored due to the limited degrees of freedom of couch motion. State-of-the-art couches can only correct rigid errors, but not compensate for curvature changes, which often occurs in neck positioning. Also, patient motions are often ignored during image-guidance procedures, where the focus is on the use of images only before treatment.

The overall goal of this work is to address the non-rigid motion compensation during H&N RT. For an initial investigation, we control the one degree of freedom, raising or lowering of a generic patient's head, lying in a supine position, to a desired height above a table. The system consists of a single inflatable air bladder (IAB), a mannequin head and a neck/torso motion simulator, Kinect Xbox 360 Sensor, two pneumatic valve actuators controlled by custom-built current regulators, and a National Instruments myRIO microcontroller. The Kinect Sensor is mounted directly above the head for displacement measurement. The error between the measured and desired head position, as sensed by the camera, is used in a PI controller nested within a PID feedforward to control the pneumatic actuator valves, thereby regulating air pressure within the IAB and moving the patient's head.

Soft robot systems are deformable polymer enclosures with fluid-filled chambers that enable manipulation and locomotion tasks by a proportional control of the amount of fluid in the chamber [11], [12]. Their customizable, deformable nature and compliance make them suitable to biomedical applications as opposed to rigid and stiff mechanical robot components – impractical in enabling articulation of human body parts. Our final design is a deformable IAB and a soft-robotic actuator specifically to address the problem deflection or attenuation of radiation beams.

The paper is structured as follows: Section II gives an

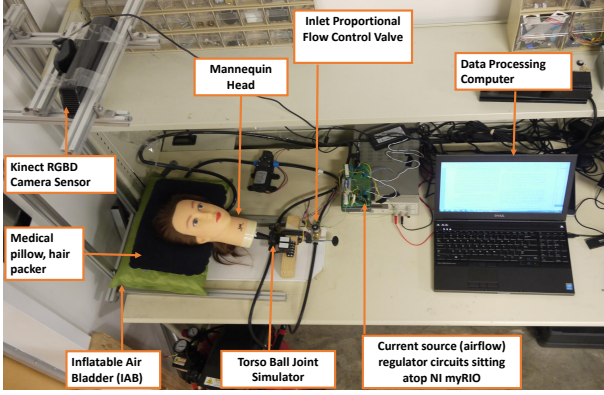


Fig. 1: Experimental Testbed

overview of the system design and hardware set-up; Section III details the vision algorithm used to determine the position of the patient's head; Section IV describes the identification of the soft robot model, and the control system design is presented in Section V. Experimental results are presented in Section VI and we discuss future work and conclude the paper in Section VII.

II. SYSTEM DESIGN

The system set-up is shown in Fig. 1. The patient simulator is a Lexi cosmetology mannequin head (11" high, 6" wide) with a hollow base that allows for a placeholder clamp. To simulate torso-induced neck motion, we attach a ball joint in the hollow base of the head. The soft robot actuation mechanism combines an inflatable air bladder (19" x 12") made of lightweight, durable and deformable polyester and PVC, two current-controlled proportional solenoid valves (Model PVQ33-5G-23-01N, SMC Co., Tokyo, Japan), and a pair of silicone rubber tubes (attached to a T-port connector at the orifice of the IAB) in order to convey air in/out of the IAB. A 1HP air compressor supplied regulated air at 30 psi to the inlet actuating valve, while an interconnection of a 60W micro-diaphragm pump and a PVQ valve removed air from the outlet terminal of the IAB. The diaphragm pump creates the minimum operational differential pressure required by the outlet valve.

We mount a Microsoft Kinect RGBD camera at approximately 710mm above the manikin head, with the IAB fully deflated. A medical pillow surrounds the head to reduce infra-red wavelengths scattering caused by the hair on the mannequin head, improve image processing for face extraction and negate undesirable head rotations. The vision algorithm was implemented on a 32GB RAM DELL Precision Laptop that ran 64-bit Windows 7.1 on an Intel Core i7-4800MQ processor. The real-time control processing was implemented on a National Instruments myRIO embedded system running LabVIEW 2014.

III. VISION-BASED HEAD POSITION ESTIMATION

The Kinect camera, though insufficient for clinical use, is reasonable for development and laboratory testing. H&N Radiotherapy verification and validation experiments will



Fig. 2: Depth Constrained 3D Face Tracking of a human head (left) and a mannequin head (right) using AAM.

incorporate the high-precision VisionRT 3D surface¹ imaging system, approved for clinical use and capable of capturing a patient's position with the sub-millimeter spatial and sub-degree rotational accuracy. We use the near mode depth range of the Kinect sensor, i.e. 400mm – 3000mm [13], and the 640 × 480 depth image resolution and stream images at 30 frames per second. We adopted the Microsoft Kinect SDK version 1.5.2 and OpenNI .NET framework [14], [15] for rapid prototyping of the experimental testbed.

An active appearance model (AAM) [16] was employed for face tracking, as it is a fast and robust method that uses statistical models of shape and gray-level appearance of faces. We adopted Smolyanski et al's approach [17], which uses depth data to constrain a 2D + 3D AAM fitting. The approach in [17] was extended to a non-human object, i.e. the mannequin head in Fig. 1, by initializing the face tracker with a qualitatively determined region of interest. The face tracker utilizes both depth and color data but computes 3D tracking results in the video camera space. The video camera space is a right-handed system with the Z-axis pointing towards the face being tracked and the Y-axis pointing in the vertical direction.

The points corresponding to the tip of the nose is fairly invariant to movement of facial muscles. Therefore, the Z-coordinates of points corresponding to the nose area were averaged, and this was used to determine the patient position with respect to the origin of the camera frame. We mapped this result to world space, i.e. the head's displacement above the table using the relation

$$y(t) = y_m - y_h \quad (1)$$

where $y(t)$ is the displacement of the head from the table; y_m is the head displacement as measured by the camera; y_h is the mounting height of the camera above the table.

The tracked head position value from (1) was transferred from the vision processing workstation to myRIO over a local wireless network using the user datagram protocol (UDP). We chose UDP over other handshaking, dialog-based connection transmission models because the application is a real-time sensitive one. The typical problem of dropped packets with UDP-based connections, is preferable for our goals over delayed packets, which can occur in other connection-based protocols. An algorithm for Network interface level

¹Vision RT – AlignRT Real-Time Patient Tracking, Patient Set-up in Radiation Therapy

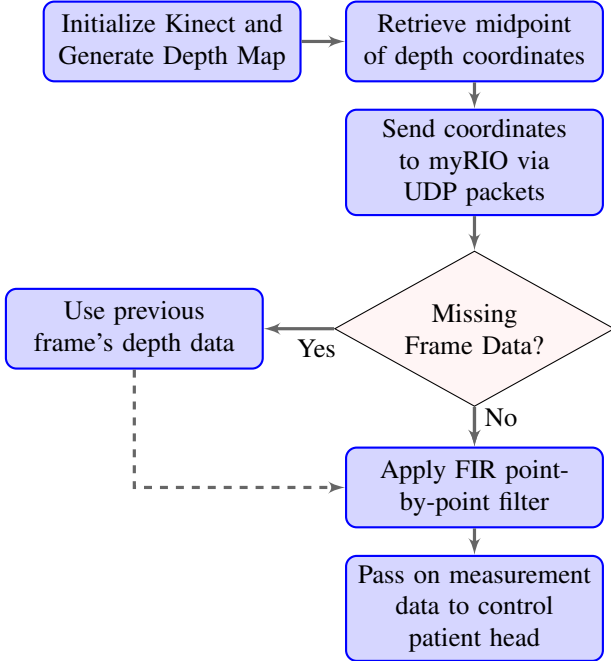


Fig. 3: Vision Flowchart Using the OpenNI .NET Assembly

error-checking and correction was handled in myRIO using the procedure described in Fig. 3.

A deterministic protocol was implemented on myRIO to prioritize transmission of Kinect measurement data and to eliminate synchronization errors between the server and the client – a common issue with the Windows operating system. To ensure the deterministic task does not monopolize other myRIO processor resources, a timing engine was employed with an execution rate equal to that of the depth image processing loop on the Windows workstation, i.e. 30Hz. Finally, a 20th order nonrecursive point-by-point finite-impulse response filter was employed to mitigate measurement noise from streamed data.

IV. SYSTEM IDENTIFICATION AND MODELING

A reliable system model is necessary to design a stable controller with required time and precision characteristics.

A. Data Collection

With the regulated air canister providing a constant pressure of 30 psi, a periodic, persistently exciting input current in the form of a sawtooth waveform was used to excite the inlet PVQ valve such that the experiment was open-loop informative [18, p. 414]. Airflow out of the outlet valve was kept constant by opening it to the mid-position of its operating range. This varied the head position through an open-loop inflation/deflation process of the IAB.

The current to the inlet valve, $u(t)$, was band-limited such that it had no power above 10Hz, i.e., the Nyquist frequency of the valves, and its spectrum coincided with the spectrum of the discrete time signal. The output signal, $y(t)$, is the height of the head given by (1). We acquired 8,800 samples of the input and output signals for data modeling, and a second set of 8,800 samples was collected for model validation.

B. Data Pre-Processing and System Model Identification

Consider a single input, single output relationship in the form of a linear difference equation

$$y(t) + a_1 y(t-1) + \cdots + a_n y(t-n) = b_1 u(t-1) + \cdots + b_m u(t-m) \quad (2)$$

Rewriting (2) such that it models a one-step-ahead predictor, we have

$$y(t) = -a_1 y(t-1) - \cdots - a_n y(t-n) + \cdots + b_1 u(t-1) + b_m u(t-m). \quad (3)$$

We want a model structure from the collected data set, $Z^N = \{u(1), y(1), \dots, u(N), y(N)\}$, parametrized by mapping from the set of all past inputs and outputs, Z^{t-1} , to the space of the model outputs. Denote the model as $\hat{y}(t|\theta)$

$$\hat{y}(t|\theta) = g(\theta, Z^{t-1}) \quad (4)$$

where θ is the set of estimated coefficients to satisfy (2)

$$\theta = [a_1 \ \dots \ a_n \ b_1 \ \dots \ b_m]^T. \quad (5)$$

The identification goal is to identify the best model in the set, Z^N , guided by frequency distribution analysis. Removing means and linear trends in collected data will minimize the effects of disturbances that are above the frequencies of interest to system dynamics, and will eliminate occasional outliers and non-continuous records in collected data [18, Ch. 3, pp. 414]. Therefore, acquired data was normalized using

$$u_{ave}(t) = u(t) - \bar{u}, \quad y_{ave}(t) = y(t) - \bar{y} \quad (6)$$

where $\bar{u} = \frac{1}{N} \sum_{t=1}^N u(t)$ and $\bar{y} = \frac{1}{N} \sum_{t=1}^N y(t)$ are the corresponding sample means, n is the discrete time index and N is the total data length [18, Ch. 1]. Linear trends were then removed using

$$u_d(t) = u_{ave}(t) - A\theta_u, \quad y_d(t) = y_{ave}(t) - A\theta_y \quad (7)$$

where θ_u and θ_y are the solutions to the least-square fit equations

$$(A^T A)\theta_u = A^T u, \quad (A^T A)\theta_y = A^T y \quad (8)$$

and

$$A^T = \begin{bmatrix} 1 & 1 & \cdots & 1 & 1 \\ \frac{1}{N} & \frac{2}{N} & \cdots & \frac{N-1}{N} & 1 \end{bmatrix}. \quad (9)$$

To examine, the relationship between the input and output signals, the normalized cross-correlation function (CCF) between $u(t)$ and $y(t)$, was determined as

$$\psi_{uy}(\tau) = \frac{\sum_{t=\tau+1}^N [u(t-\tau) - \bar{u}] [y(t) - \bar{y}]}{\sqrt{\sum_{t=1}^N [u(t) - \bar{u}]^2} \sqrt{\sum_{t=1}^N [y(t) - \bar{y}]^2}} \quad (10)$$

$$\tau = 0, \pm 1, \dots, \pm (N-1).$$

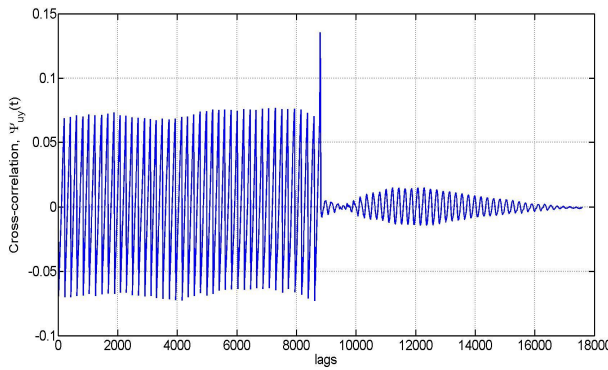


Fig. 4: CCF of Input and output Signals

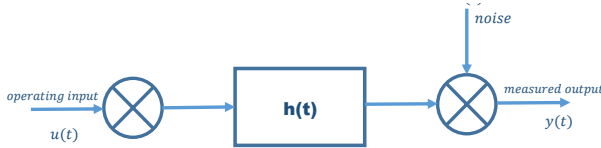


Fig. 5: Impulse Response Correspondence with the CCF

Since the CCF is the convolution of the system impulse response, $h(t)$ and the process auto-correlation function, $\phi_{uu}(t)$, the Wiener-Hopf equation (10) can be rewritten as

$$\begin{aligned}\psi_{uy}(\tau) &= \int h(\nu)\mathbb{E}[u(t)u(t+\tau-\nu)]d\nu \\ &= \int h(\nu)\psi_{uu}(\tau-\nu)d\nu\end{aligned}\quad (11)$$

where \mathbb{E} denotes the expectation operator. Equation (11) implies the CCF between the output and test input is proportional to the system impulse response when the input is a white noise signal[18, p. 13]. The CCF in Fig. 4 is not a correct estimate of the system impulse response, since the excitation input was not a white noise sequence. Therefore, the input and output were prewhitened with a white noise input sequence, $u_{pw}(t) = u(t)F(z^{-1})$, where $u_{pw}(t)$ is a zero-mean white input sequence and $F(z^{-1})$ is an autoregressive filter of order 20 defined as

$$F(z^{-1}) = 1 + \varsigma_1 z^{-1} + \varsigma_2 z^{-2} + \dots + \varsigma_{20} z^{-20}. \quad (12)$$

The parameters ς_i , ($i = 1, 2, \dots, 20$) were estimated by fitting an autoregressive model to $u(t)$ and were generated with the ‘ar’ command in MATLAB.

The estimation result after fitting the white noise autoregressive model was found to have 76.75% fit to estimation data, with a mean squared error (MSE) of 78.11 mm². The normalized auto-correlation function tells of the filter quality $F(z^{-1})$ and is given by

$$\psi_{uu}(\tau) = \frac{\sum_{t=1}^N [u(t) - \bar{u}][u(t+\tau) - \bar{u}]}{\sum_{t=1}^N [u(t) - \bar{u}]^2} \quad (13)$$

where $\tau = 0, \pm 1, \dots, \pm(N-1)$.

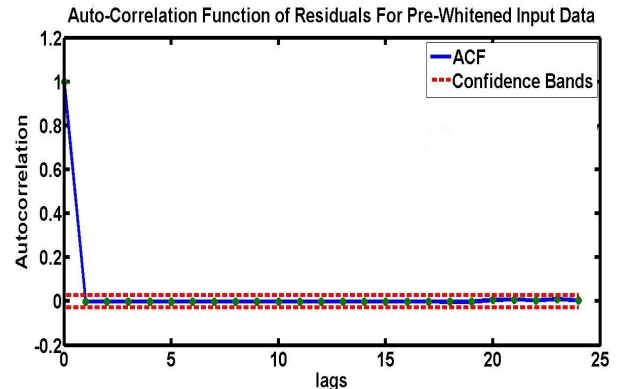


Fig. 6: Correlation Function of Residuals

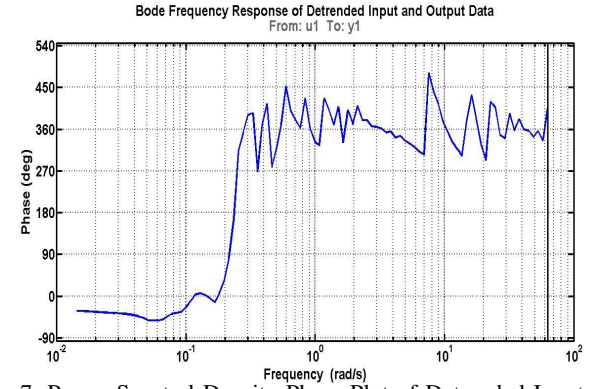


Fig. 7: Power Spectral Density Phase Plot of Detrended Input and Output Signals

The auto-correlation function of the residuals of the pre-whitened input signals, seen in Fig. 6, are within 95% confidence bands (the dashed red lines). Hence, we conclude that we correctly estimated the filter. To find an optimal sub-model for the identified system that will tolerate non-linearities and handle disturbances well, our final choice was a linear, second-order grey-box process model on the detrended data with quality measurable by the MSE. This model choice is informed by the previous impulse response analysis which suggests a delay in the system (Fig. 6) and gave an affordable model cost acceptable for solving $\hat{\theta}_N$. A high-order complex model may be marginally better but may not be worth the higher cost [18, §16.8].

By analyzing the bode response of the spectral frequency density distribution of the detrended data, we chose the approximately linear frequency range (0.00232 rad/sec – 6.85 rad/sec) in the frequency distribution of Fig. 7 to represent the desired model.

C. Model Estimation

Using term selection and parameter estimation, we fit a second-order process model with transfer function form

$$G(s) = K_p \frac{1 + sT_z}{(1 + sT_{p_1})(1 + sT_{p_2})} e^{-sT_d}. \quad (14)$$

where T_z , T_{p_1} , and T_{p_2} are respectively the process zero and the time constants contributed by the first and second pole of the system; K_p is the process dc gain, and T_d is the process

dead time. The delay is a result of the non-collocation of the sensor and actuator. The identified parameters of (14) are listed in Table I.

TABLE I: Parameter Estimation Results for Soft Robot System

K_p	T_z	T_{p1}	T_{p2}	FPE	MSE	T_d
1.0015	-0.58354	100	9.7257	1.672	0.05498	2

A first-order measurement noise component ARMA disturbance model, has been fit into $G(s)$

$$y(s) = G(s)u(s) + \frac{C(s)}{D(s)}e(s), \quad (15)$$

where $e(s)$ is a white noise, $C(s) = s + 899.3$, and $D(s) = s + 7.789$. A prediction focus was used to weigh the relative importance of how closely to fit the data in the various frequency ranges. This favored the fit over a short time interval [22, Ch. 3, Sec. 3-38]. The model has 87.35% fit to original data with improved quality as the final prediction error (FPE) and MSE shows.

D. Residual Analysis

To verify the model accuracy with respect to our control goal, we employed canonical analysis by computing the prediction errors as a frequency response from the inputs to the residuals not picked up by the model. Defining the outputs predicted by the model as $\hat{y}(t|\hat{\theta})_N$, the errors from the modeling process are the residuals

$$\alpha(t) = \alpha(t, \hat{\theta}_N) = y(t) - \hat{y}(t|\hat{\theta})_N. \quad (16)$$

A basic statistics for the residuals from the model such as

$$S_1 = \max_t |\alpha(t)|, \quad S_2^2 = \frac{1}{N} \sum_{t=1}^N \alpha^2(t) \quad (17)$$

will inform us about the model's quality since the upper limit of S_1 or the average error of S_2 for all data we have will also be bound for all future data. In order to check that the model would work for a range of possible inputs, we study the covariance between residuals and past inputs

$$\hat{R}_{\alpha u}^N(\tau) = \frac{1}{N} \sum_{t=1}^N \alpha(t)u(t-\tau) \quad (18)$$

and deem the model is invariant to other inputs if the numbers, $\hat{R}_{\alpha u}^N(\tau)$, are small enough so that $y(t)$ could not have been better predicted, i.e., there is no part of $y(t)$ not picked up by the model $G(s)$. We compare the estimates of the obtained linear model with the corresponding standard deviation (from the validation data set, Z_v^N) in Bode plots with estimated variance translated to confidence intervals. We see from Fig. (8) that the model's frequency response generally stays within the 99% confidence bands (the pink and purple lines), and conclude we have a reliable model.

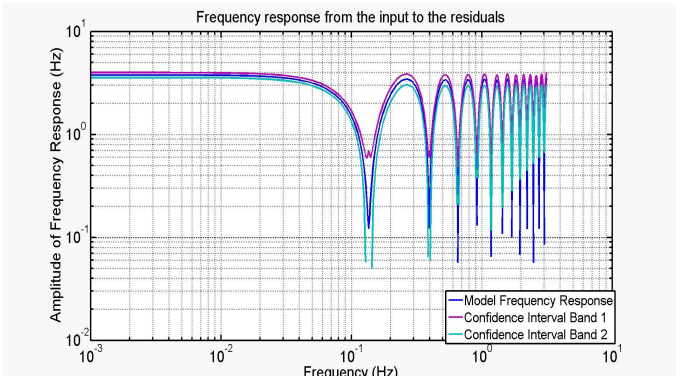


Fig. 8: Frequency analysis from past inputs to residuals

V. CONTROL DESIGN

The step response of the open loop system (Fig. 9) shows the system is stable, but with a very slow transient response. We require a controller that gives closed loop stability and achieves a clinically acceptable response time (15 - 30 seconds) while balancing the trade-off between aggressiveness and robustness. To do this, a pole was added at the origin and a zero was kept close to the introduced pole as in Fig. 12 using the following PI-controller in a feedforward configuration with obtained model.

$$G_c = 3.79 + \frac{0.0344}{s}. \quad (19)$$

This reduced steady state error while maintaining transient characteristics. The closed-loop unit step response with the added controller is shown in Figure 10. The system's transfer function with the added PI controller of (19) is

$$G_{ol} = \frac{-0.00228(s + 0.009073)(s - 1.7137) \exp^{-2s}}{s(s + 0.01)(s + 0.1028)} \quad (20)$$

where the delay was approximated with a second-order Padé approximant of the form

$$H(s) = \frac{s^2 - 3s + 3}{s^2 + 3s + 3}. \quad (21)$$

This preserved the transient characteristics by sufficiently approximating the delay according to our control goal. The overall desired transient and frequency response was then realized with a feedforward PID-controller in series with the closed loop network of the PI-controlled soft robot system (12). The PID controller, given by

$$G_{PID} = 3.4993 + \frac{0.054765}{s} + 55.8988s, \quad (22)$$

corrected fluctuations in air flow into the IAB and improved the system's dynamic performance such that the overall closed loop network has the step response seen in Fig. 11. This produced a non-minimum phase system with settling time of approximately 14 seconds. As seen in Fig. 11, the system converges to steady state with a rise time of 6.29 seconds. The overall PID-PI control network (shown in Fig. 12) is closed loop stable as the Bode plot of Fig. 13 shows.

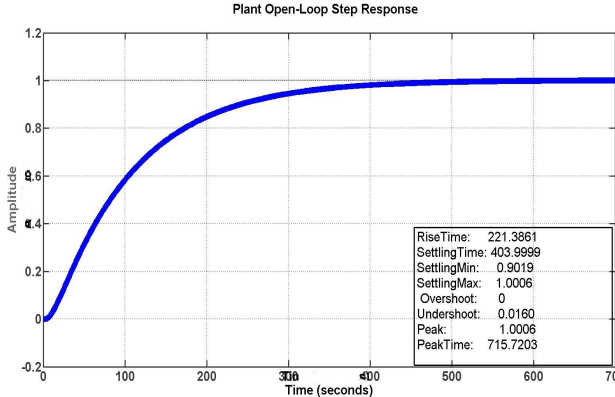


Fig. 9: Open-Loop Step Response of Identified Model



Fig. 10: Closed-Loop Step Response of PI tuned Soft Robot System

VI. EXPERIMENTAL VALIDATION

The testbed of Fig. 1 was used to validate the proposed model and control network. The control algorithm was implemented using a Runge-Kutta second-order ordinary differential equation solver that ran on the myRIO at a fixed step size of 0.1 second. A fixed step solver was used to avoid reduction in computational efficiency in having to discretize the controller and soft robot model, which were both modeled in the continuous-time domain. To ensure the deployment was executed in real-time, the timing source of the execution loop on the Windows workstation was also synchronized to the myRIO hardware.

Experimental results with constant reference tracking is shown in Fig. (14). With a constant set-point target of 25.32cm above the table, and the manikin head being 24.51cm above the table at rest position, the algorithm was deployed to track the set-point trajectory. The controller behaves as expected, reaching within 2% of the reference after a rise time of approximately 15 seconds and tracking the setpoint trajectory to within 0.2cm maximum deviation. The system also displays less overshoot and clinically acceptable settling time. A second experiment (Fig. 15)with changing set-points was carried out. The controller tracks the set-point trajectories with a maximum deviation of 2mm from setpoint.

The depth and range resolution of the Kinect Xbox sensor accounts for the deviation from setpoint trajectory when the

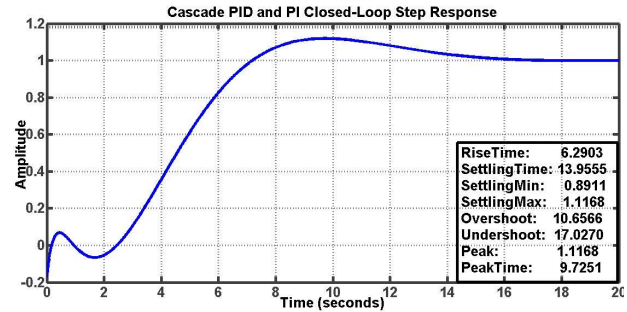


Fig. 11: Closed Loop Step Response Plot of PID and PI Cascade Network

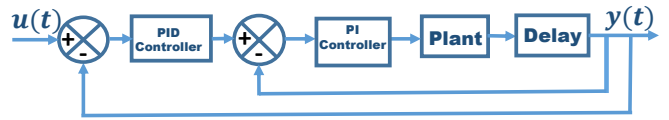


Fig. 12: Block Diagram of Model

controller is applied. The chosen set-points of figures (14), and (15) are extensible for use in target clinical applications as a typical H&N RT may demand. Future multi-axis head positioning work will explore the new time-of-flight based Kinect for Windows v2 sensor which has an improved noise floor, visualizes small objects in greater detail and more clearly, and a depth fidelity of 512×424 pixels and a wider field of view (fov) of 70.6×60 degrees compared with the 320×240 pixels with 58.5×46.6 degrees fov of the Xbox sensor used in this work.

VII. CONCLUSIONS

Accurate positioning of the patient head and torso is crucial in intensity modulated radiotherapy. Deviations from desired positions have been known to cause dose variation, degenerate treatment efficacy, brain necrosis and edema[3]. In this paper, the control of cranial flexion/extension motion of a patient during maskless and frameless, image-guided

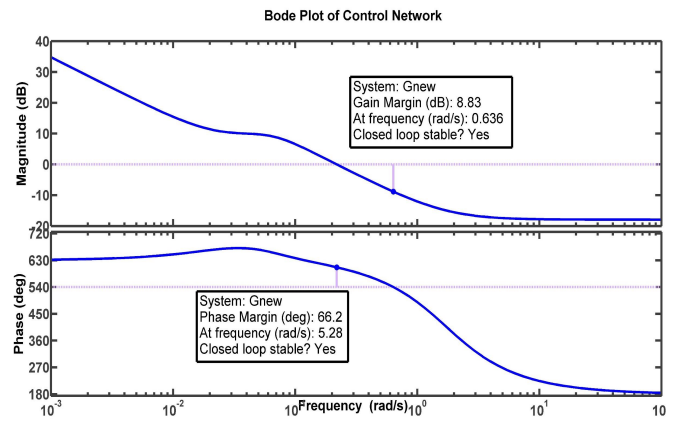


Fig. 13: Bode Response Plot of feedforward and Cascade Control Network

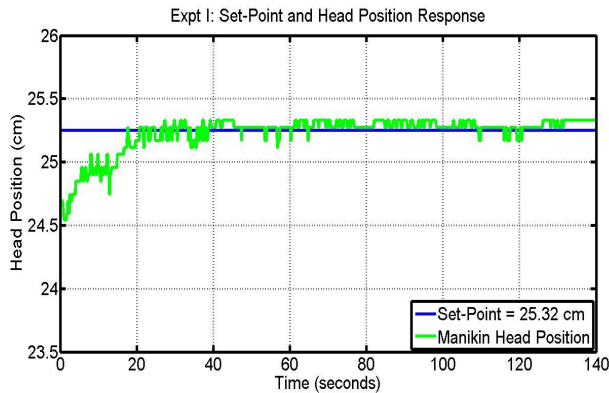


Fig. 14: Manikin head response to a constant setpoint

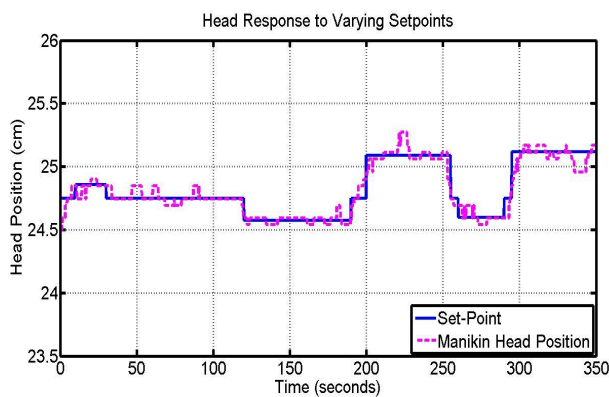


Fig. 15: Varying Set-points and Manikin Head Trajectory Tracking

radiotherapy was considered using a manikin head as a test subject. We established that the proposed soft robot can track a desired step reference trajectory with 2mm precision after a lag time of 15 seconds. This was achieved using a PI controller nested within a PID feedforward configuration and implemented on an NI myRIO. The Kinect Xbox 360 sensor sensed head position.

This shows the possibility of accurate positioning with the choice of a deliberate, well-tuned controller. Future efforts will focus on designing a more accurate and robust controller usable for clinical RT and improve the transient characteristics. We will also look into gain scheduling to allow different settling times for different motion, as fast motions may be uncomfortable for patients. Long term efforts include extending the results to the deformable motions of the upper torso, and H&N. This would involve multiple bladders, finding the coupling needed between IABs to give desired actuation, refining the system model for the bladders, and developing a more accurate and robust controller, in order to achieve multi-axis positioning irrespective of patient head shape or size. This would demonstrate comprehensive and accurate automated control of a patient's position during cancer H&N radiotherapy, prevent unwanted anatomical deformations and other harmful effects that positioning deviations have been known to cause.

REFERENCES

- [1] Siegel, R., et al., Cancer statistics, 2014. CA: A Cancer Journal for Clinicians, 2014. 64(1): p. 9-29.
- [2] Xing, L., Dosimetric effects of patient displacement and collimator and gantry angle misalignment on intensity modulated radiation therapy. Radiother Oncol, 2000. 56(1): p. 97-108.
- [3] Takakura, T., et al., The geometric accuracy of frameless stereotactic radiosurgery using a 6D robotic couch system. Phys Med Biol, 2010
- [4] Ahn, P.H., et al., Random positional variation among the skull, mandible, and cervical spine with treatment progression during head-and-neck radiotherapy. Int J Radiat Oncol Biol Phys, 2009. 73(2): p. 626-33.
- [5] D. Robb, A. Plank, and M. Middleton, Assessing the Efficiency and Consistency of Daily Image-guided Radiation Therapy in a Modern Radiotherapy Centre. Journal of Medical Imaging and Radiation Sciences, 2013.
- [6] Gevaert, T., et al., Setup accuracy of the Novalis ExacTrac 6DOF system for frameless radiosurgery. Int. J. Radiation Oncology Biol. Phys. Vol. 82, No. 5, pp. 1627-1635, 2012.
- [7] Cervino, L.I., Pawlicki, T., Lawson, J.D., Jiang, S.B., Frame-less and mask-less cranial stereotactic radiosurgery: a feasibility study. Phys. Med. Biol. 55 (2010) 1863-1873.
- [8] Manning, M.A., et al., The effect of setup uncertainty on normal tissue sparing with IMRT for head-and-neck cancer. Int J Radiat Oncol Biol Phys, 2001. 51(5): p. 1400-9.
- [9] Hong, T.S., et al., The impact of daily setup variations on head-and-neck intensity-modulated radiation therapy. Int J Radiat Oncol Biol Phys, 2005. 61(3): p. 779-88.
- [10] Den, R.B., et al., Daily image guidance with cone-beam computed tomography for head-and-neck cancer intensity-modulated radiotherapy: a prospective study. Int J Radiat Oncol Biol Phys, 2010. 76(5): p. 1353-9.
- [11] C. Laschi, et al., Soft robot arm inspired by the octopus. Advanced Robotics, 2012. 26(7): p. 709-727.
- [12] P. Maeder-York, et al., Biologically Inspired Soft Robot for Thumb Rehabilitation. Journal of Medical Devices, 2014. 8(2): p. 020933-020933.
- [13] Constants [Online]. Available: <https://msdn.microsoft.com/en-us/library/hh855368>
- [14] Microsoft Kinect for Windows SDK v1.5.2 [Online]. Available: <http://www.microsoft.com/en-us/download/details.aspx?id=30455>
- [15] Simple-OpenNI. OpenNI Library for Processing [Online]. Available: <https://code.google.com/p/simple-openni/>
- [16] G.J. Edwards, C.J. Taylor, and T.F. Cootes, Interpreting Face Images using Active Appearance Models. In Proc. Third IEEE International Conference on Automatic Face and Gesture Recognition, 1998 300 -305
- [17] N. Smolyanskiy, C. Huitema, L. Liang, S.E. Anderson, Real-time 3D face tracking based on active appearance model constrained by depth data. Image and Vision Computing 32 (2014) 860-869
- [18] L. Llungs, *System Identification Theory for the User*. 2nd Edition. Upper Saddle River, NJ, USA. Prentice Hall, 1999.
- [19] J. Xiao, S. Baker, I. Matthews, T. Kanade, Real-time combined 2D + 3D active appearance models, Computer Vision and Pattern Recognition (2004) 535 -542.
- [20] Microsoft.Kinect Namespace [Online]. Available: <https://msdn.microsoft.com/en-us/library/microsoft.kinect.aspx>
- [21] H.L. Wei, Q.M. Zhu, S.A. Billings. System Identification Using Matlab. Department of Automatic Control and Systems Engineering, The University of Sheffield, Sheffield, UK. August 2002.
- [22] L. Llungs, *System Identification ToolboxTM User's Guide R2014b*. The MathWorks, Inc. Natick, MA. 2014.